Experimental and Numerical Investigation of Air Radiation in Superorbital Expanding Flow

Han Wei*, Richard G. Morgan†, and Timothy J. McIntyre‡
The University of Queensland, St Lucia, Queensland, 4072, Australia
Aaron M. Brandis§
AMA at NASA Ames Research Center, Mountain View, CA, 94035, USA
and
Christopher O. Johnston¶
NASA Langley Research Center, Hampton, VA, 23681, USA

To investigate air radiation in expanding flows and provide experimental data for validating associated computational models, experiments were conducted in the X2 expansion tunnel facility at the Centre for Hypersonics of the University of Queensland. A 54° turning angle wedge model was employed to generate steady expanding flows with inflow total enthalpies of 50.7, 63.4 and 75.4 MJ/kg. VUV spectra from 118 to 180 nm were acquired across the wedge at three equispaced distances away from the top of the model, as well as through its top surface. High speed filtered images were also obtained by coupling a Shimadzu 1 MHz high speed camera to a bandpass filter to obtain calibrated images of the 777 nm oxygen triplet. Both the across-wedge VUV spectra and filtered images of the 777 nm atomic oxygen were compared with NEQAIR simulations, which were performed using flow field data from two-dimensional CFD simulations with two-temperature 11-species air chemistry utilising the in-house Navier-Stokes flow solver Eilmer3.

Data extracted from consecutive frames of the filtered high speed images confirmed up to 8 µs of available test time for the flow conditions tested. For the strongly radiating 149 and 174 nm atomic nitrogen lines, large disagreement between experimental data and NEQAIR predictions can be observed from the start of the expansion fan where the electron-ion recombination process commences. The spatial extent, or spans of the radiance profiles of the 149 and 174 nm N lines are significantly underpredicted by NEQAIR, and are very close to those of N, N^+ and electron number density profiles, which follow that of flow density. The electron-ion recombination process is proposed as the main reason for these discrepancies. The comparisons between NEQAIR simulations and filtered images of the 777 nm oxygen triplet show good agreement in the post-shock compression region and the start of the expansion fan for the 63.4 MJ/kg condition, but with up to a factor of three overprediction by NEQAIR further downstream, which is attributed to electron-impact excitation. Similar trends are found with the 75.4 MJ/kg condition, with reduced level of agreement in the compression region, which can be due to uncertainties in inflow condition.

I. Introduction

RADIATIVE heating is a critical design consideration for the forebody thermal protection system (TPS) of a vehicle entering the Earth's atmosphere at superorbital speeds.[1,2] With state-of-the-art computational models, afterbody thermal load is found to be dominated by radiation at such entry velocities.[3] This can

*PhD Candidate, Centre for Hypersonics, School of Mechanical and Mining Engineering.
†Director, Centre for Hypersonics, School of Mechanical and Mining Engineering, Associate Fellow AIAA.
‡Head of Physics, School of Mathematics and Physics, Member AIAA.
§Senior Research Scientist, Aerothermodynamics Branch, Senior Member AIAA.
¶Aerospace Engineer, Aerothermodynamics Branch, Member AIAA.

have severe implications particularly for the future Mars return mission which requires a vehicle with a large surface area and a high entry velocity. Compared with their forebody counterparts, the afterbody heat shields in past missions bore larger safety margins[4] to account for the considerable uncertainties in computational models that were used to generate the baseline designs. The sparsity of relevant model validation data is a major source of such uncertainties.[4]

The most remarkable measurements of afterbody radiation at superorbital entry velocities were made during the flights of FIRE II[5] and Apollo 4.[6] With no discernible data recorded by the afterbody radiometers, the conclusion was made that no radiative heating was experienced on the conical section[6] of the Apollo Command Module. Post-mission analysis by Wright et al.[7] with modern computational fluid dynamics (CFD) models achieved excellent agreement with forebody convective heating data, but the afterbody experimental data were a factor of two higher than the noncatalytic predictions. By including finite rate catalysis in the simulations, improvement was only achievable in the early part of the trajectory, and pyrolysis was proposed as the possible mechanism responsible for such discrepancies. Johnston and Brandis[3] re-examined the FIRE II afterbody measurements and questioned the performance of the radiometers, given that no radiative heating was measured in the afterbody region. They analysed radiation along a constant-property line of sight with typical afterbody flow properties, observed and explained the dominance of VUV radiation in the afterbody, and identified major sources of model uncertainties for afterbody radiation, including the rate coefficient for the three-body electron-ion recombination reaction, the escape factors on collisional-radiative modelling, and the impact of forebody ablation.

More recently, Johnston and Panesi[8] made improvements to the modelling of afterbody radiation, including treating nitrogen atoms of different grouped electronic levels as individual species in the flow field model, coupling radiative transition rates to the species continuity equations, adopting a ray-tracing approach in radiation transport calculation and developing a nonequilibrium model for NO. Lopez, Johnston and Panesi[9] improved the non-Boltzmann modelling of nitrogen by adopting a state-to-state description of grouped electronic states. West, Johnston and Hosder[10] performed sensitivity analysis and uncertainty quantification of afterbody radiation associated with the Stardust re-entry capsule at peak afterbody radiative heating conditions. Out of the 388 parameters used in the uncertainty analysis, four variables were found to contribute to nearly 95% of the uncertainty. They are the electronic-impact excitation rate for N between levels 2 and 5, as well as the chemical reaction rates affecting the number densities of N, N^+, O and O^+. With these improvements made in the computational models for afterbody radiation relevant to superorbital Earth entry, validation data of afterbody radiation, particularly in the VUV wavelength range is in high demand.

II. Experiments

A. Test Model

The test model is presented in Figure 1. The front wedge faces the test flow, and an attached shock wave is formed due to its presence. The flow is first strongly compressed and decelerated by the shock, and then expands and accelerates through the expansion fan emanating from the ramp corner. The downstream end of the shock wave is attenuated due to its interaction with the expansion fan, as is indicated by the gradually more oblique shock angles.

Dissociation occurs in the post shock region and approaches completion over a short distance for the high enthalpy test conditions. The shock layer is thus populated with many electronically excited nitrogen and oxygen atoms which emit the bulk of the radiation. Ionisation is also in progress within the shock layer, yet far from complete. Entering the expansion fan, many of these atoms continue to radiate due to limited recombination rates.[3]

Two typical streamlines are defined in Figure 1. Flow along different streamlines goes through similar levels of compression and therefore comparable degrees of dissociation and ionisation owing to unified shock strength. However, dramatic differences start to occur when it comes to the expansion process. Streamlines close to the corner of the ramp, such as Streamline 1, travel through the centre of the expansion fan and experience strong expansion within a short distance. The pressure and temperature drop is rapid, and the extinction of radiation is expected to be quick.

In contrast, streamlines traversing the outer region of the expansion fan like Streamline 2, are subjected to milder expansion over a larger length scale, and consequently a more moderate density and temperature decrease, as well as a more gradual radiation attenuation. While temperature and density variation greatly

affects the rates of relaxation processes in the expanding flow, velocity gain from the expansion also dramatically alters the flow residence time, leading to dissimilar levels of thermochemical non-equilibrium along varied streamlines.

VUV spectra were acquired along the freestream direction to spatially resolve the evolution of VUV radiation. As illustrated in Figure 2, two types of measurements were made: one with flow radiation collected across the width of the model, and the other gathering radiation incident on the top surface of the model. Across-wedge spectra were acquired along lines of sight (denoted as dashed lines) across the shock wave and into the expansion fan at 3.25, 5.75 and 8.25mm away from model top, and through-surface measurements were performed along the centreline of the nozzle exit flow, starting right behind the wedge corner and reaching into the afterbody.

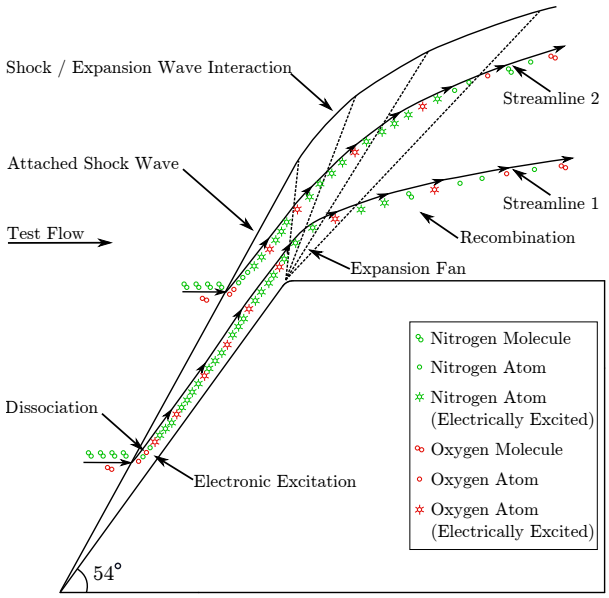

Figure 1. Schematic of the model as well as the physical processes involved

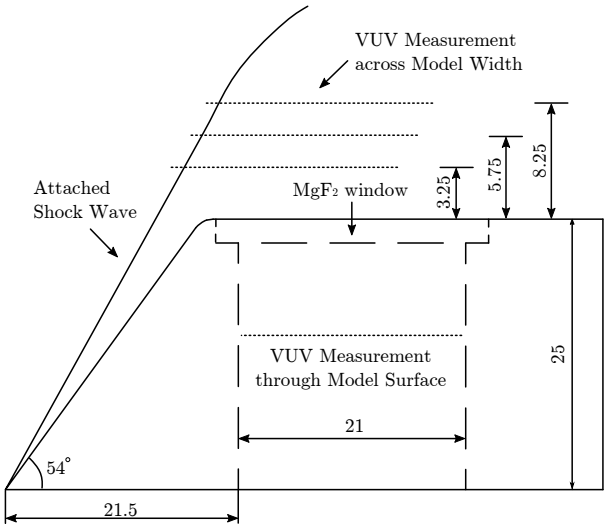

Figure 2. Schematic of across- and through-wedge VUV spectral measurements

B. Facility

The experiments were conducted in the free-piston driven expansion tunnel facility X2 located at the Centre for Hypersonics, the University of Queensland. A sketch of the approximately 25 m long facility is presented in Figure 3. The facility consists of the reservoir which contains high pressure compressed air to drive the piston, the compression tube that holds low molecular weight driver gas, typically helium or a combination of helium and argon, the shock tube in which test gas is filled, the acceleration tube connected to a Mach 10 nozzle that slides into the test section of the dump tank. Gases of different composition or pressure are segregated by diaphragms which are burst during tunnel operation. PCB® 112A22 piezoelectric pressure transducers are flush mounted on the walls of the shock tube and acceleration tube to indicate arrivals of shock waves and to measure wall pressure. Notations as well as rough locations of these pressure transducers are annotated in Figure 3.

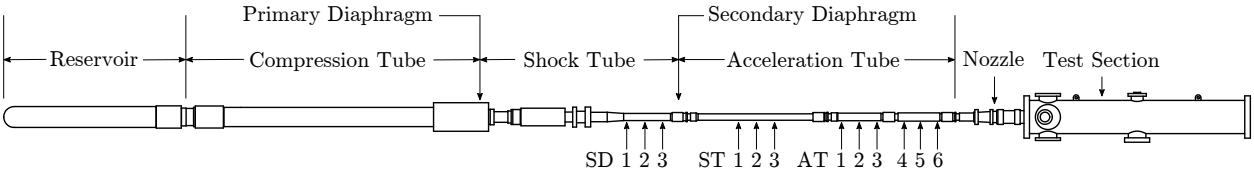

Figure 3. An illustration of the X2 expansion tunnel facility, adapted from[11]

When the piston is released, high pressure air in the reservoir accelerates it toward the low pressure driver gas in the compression tube. Piston motion compresses the driver gas and gives rise to its pressure which ultimately exceeds that behind the piston, decelerating the piston. As the piston continues to proceed inside the compression tube, the increasing driver gas pressure eventually reaches the rupture limit of the primary diaphragm (typically 2 mm pre-scored cold-rolled steel) that segregates the driver gas and the test gas. Upon primary diaphragm rupture, a strong shock wave is generated. As the primary shock traverses the test gas in the shock tube, it increases the pressure, temperature and velocity of the gas until reaching and rupturing the secondary diaphragm (normally a 0.016mm thick aluminium sheet). The primary shock can be reflected, moves upstream and further processes the test gas. The effects of the reflected shock on the flow properties in the test section depends on the condition, and is discussed in Section C. The secondary shock wave generated on the diaphragm burst travels downstream and processes the low pressure acceleration gas before exiting the nozzle. As the shock-processed test gas enters the acceleration tube, it undergoes a strong unsteady expansion and gains extra total pressure and enthalpy. The available test time starts as the test gas expands through the nozzle and reaches the test section, and ends at the arrival of any waves that disrupt the uniform test flow.[12]

C. Flow Conditions

Two conditions previously developed by Sheikh[13] to study shock layer radiation in the VUV range are employed in the current experiments. To add more value to the experiments, a third condition was designed for this campaign by James[14] so that its specific enthalpy lies between the existing ones. The three conditions are noted as Conditions 1, 2 and 3 in the order of increasing specific enthalpy. Fill pressures for these conditions are tabulated in Table 1.

Table 1. Fill pressures for the three test conditions

Condition	Driver Gas	Shock Tube (Pa)	Acceleration Tube (Pa)
1	Pure He	$3000 \pm 0.2\% + 5$	$10 \pm 0.2\% \pm 0.1$
2	90% He 10% Ar	$3000 \pm 0.2\% + 5$	$10 \pm 0.2\% \pm 0.1$
3	Pure He	$6000 \pm 0.2\% + 5$	$18 \pm 0.2\% \pm 0.1$

The same combination of reservoir and driver fill pressures of 6850 ± 50 and 92.8 ± 0.2 kPa are shared among the three conditions, although with varying driver gas compositions. The percentage uncertainties in Table 1 are based on the accuracies of the different gauges installed at the filling stations. Considering the leaking rates of the shock tube, an upper limit of 5 Pa can be superimposed on the listed shock tube fill pressure uncertainty. A ± 0.1 Pa can be applied to the acceleration tube pressure to account for leaking and operation precision, considering the operating procedure.

For experiments in which VUV spectra and filtered high speed images were acquired, the data were not only used to reveal the trends in afterbody radiation, but also to validate and calibrate existing numerical models applied in the design of heat shields. Therefore, flow condition characterisation of every specific experiment is theoretically superior to utilising a unified set of nominal parameters, and is carried out for individual experiment using the *PITOT*[14] code. It was run in the '*experiment mode*' wherein the flow properties in the shock tube were calculated with the experimentally measured primary shock speed deduced from the pressure rises detected by transducers SD1 and SD3 in Figure 3. Average static wall pressure measured in the expansion tube by transducers AT4 to AT6 was adopted in the acceleration tube calculation to obtain the properties that the shock-processed test gas was unsteadily expanded to. For conditions with which the effects of the secondary diaphragm cannot be neglected, the secondary shock speeds tend to be overpredicted. A loss factor has been defined as the ratio of the actual velocity of the shock-processed test gas and the theoretical value. The closer its value is to unity, the less effect the secondary diaphragm has on the flow property of shock-processed test gas. By adopting this factor, the shock-processed test gas was slowed down to obtain calculated secondary shock speeds that match the experiment values.

Inflow properties of three shots for the across-wedge VUV spectral measurements and one for the through-surface experiment are tabulated for each flow condition in Tables 2, 3 and 4. The primary shock speeds were measured between pressure transducers SD1 and SD3, and the secondary shock speeds were obtained between

pressure transducers AT4 and AT6. These shots are selected due to the small difference in flow properties among them. The standard deviation (SD) and coefficient of variance (CV) are also listed beside the mean value for each flow variable. The loss factor is found to decrease with increasing flow enthalpy, suggesting stronger effects of the secondary diaphragm on high enthalpy conditions. For all three flow conditions, the largest shot-to-shot variations are found in flow density and pressure, with temperature and velocity much better repeated between shots.

Table 2. Calculated and experiment flow variables for Condition 1

Flow Variable	x2s3026	x2s3031	x2s3037	x2s3056	Mean	SD	CV (%)
Expanded test gas pressure (Pa)	5220±170	6010±180	6220±460	5280±490	5680	510	8.98
Primary shock speed (m/s)	4814±38	4834±38	4854±38	4834±38	4834	16.3	0.34
Secondary shock speed (m/s)	9613±54	9577±54	9583±54	9635±54	9602	27.0	0.28
Loss factor	1.0	1.0	1.0	1.0	1.0	0	0
Test flow pressure (Pa)	1203.0	1382.0	1430.0	1217.0	1308.0	115.0	8.79
Test flow temperature (K)	2580.8	2624.1	2640.7	2591.7	2609.3	27.9	1.07
Test flow velocity (m/s)	9741.1	9663.1	9677.2	9775.6	9714.3	53.1	0.55
Test flow density (g/m^3)	1.56	1.76	1.80	1.57	1.67	0.13	7.49
Total enthalpy (MJ/kg)	50.91	50.29	50.49	51.29	50.74	0.44	0.87

Table 3. Calculated and experiment flow variables for Condition 2

Flow Variable	x2s3028	x2s3033	x2s3042	x2s3059	Mean	SD	CV (%)
Expanded test gas pressure (Pa)	10860±1920	10990±1590	12630±980	11530±1630	11500	810	7.71
Primary shock speed (m/s)	5369±44	5344±44	5419±45	5394±45	5381	32	0.60
Secondary shock speed (m/s)	10690±60	10698±60	10755±61	10797±61	10735	50	0.47
Loss factor	0.97	0.98	0.98	0.98	0.98	0.005	0.51
Test flow pressure (Pa)	1438.0	1456.0	1664.0	1523.0	1520.3	102.6	6.75
Test flow temperature (K)	2695.1	2689.4	2749.7	2718.6	2713.2	27.4	1.01
Test flow velocity (m/s)	10885.3	10864.4	10910.1	10936.4	10899.1	31.1	0.29
Test flow density (g/m^3)	1.76	1.79	1.98	1.84	1.84	0.097	5.29
Total enthalpy (MJ/kg)	63.17	62.91	63.65	63.82	63.38	0.421	0.66

Table 4. Calculated and experiment flow variables for Condition 3

Flow Variable	x2s3022	x2s3036	x2s3044	x2s3060	Mean	SD	CV (%)
Expanded test gas pressure (Pa)	7680±410	9390±410	8020±240	7480±930	8140	860	10.6
Primary shock speed (m/s)	6036±53	5944±52	5974±52	5944±52	5975	44	0.73
Secondary shock speed (m/s)	11708±66	11522±65	11740±66	11509±65	11620	121	1.04
Loss factor	0.930	0.970	0.970	0.930	0.950	0.023	2.43
Test flow pressure (Pa)	790.4	965.5	832.1	784.4	843.1	84.3	10.00
Test flow temperature (K)	2897.2	2918.4	2889.3	2863.4	2892.1	22.7	0.79
Test flow velocity (m/s)	11929.0	11729.1	11955.4	11735.2	11837.2	121.8	1.03
Test flow density (g/m^3)	0.84	1.03	0.89	0.85	0.91	0.086	9.47
Total enthalpy (MJ/kg)	76.55	74.19	76.79	74.07	75.40	1.5	1.95

D. Optical Emission Spectroscopy

A top view of the experiment layout in the test section including the VUV optical emission spectroscopy system is presented in Figure 4, which is based on that initially set up by Sheikh.[13] The original system consists of two sections connected by a flexible high vacuum bellows: the height-adjustable optics table and the light tube attached to the side flange of the test section, which is employed to minimise loss of VUV

radiation due to absorption. On the table is the optics box enclosing the mirrors, and the Andor™ iStar DH340T ICCD camera attached to the McPherson™ Nova 225 1 m focal length VUV spectrometer. The camera sensor is a 2048×512 array of 13.5 µm sized pixels. The diameter of the image intensifier is 18 mm, which gives an effective resolution of 1330×512 pixels, with 512 pixels distributed along the spatial axis of the spectral image. With the 300 lines/mm grating used, a spectral resolution of roughly 0.05 nm/pixel is achieved.

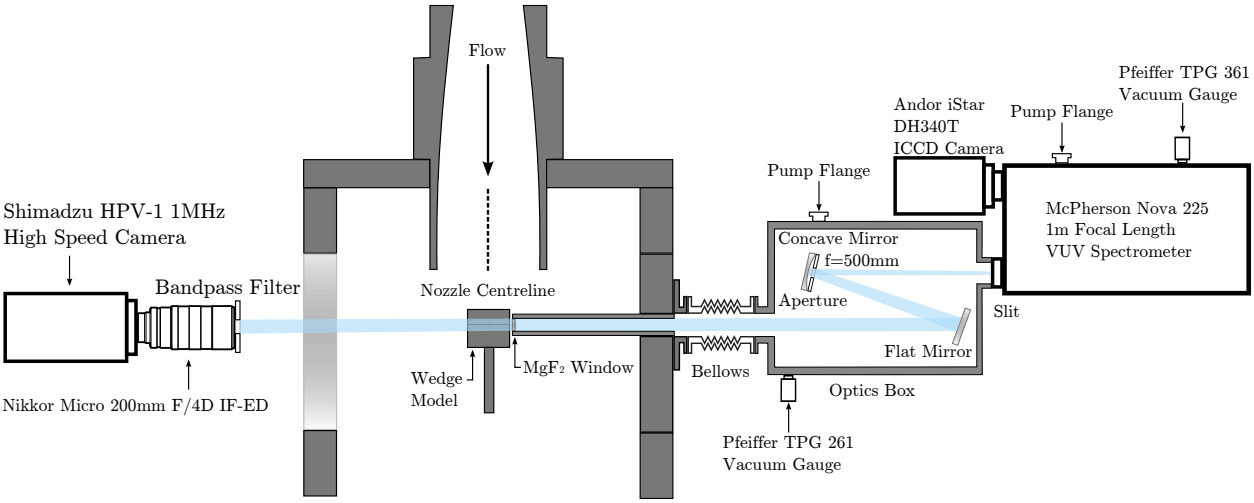

Figure 4. Top-view of the entire optical measurement system (not in scale)

VUV spectral measurements across the width of the wedge and through its shoulder were made with the same optical emission system. This was realised by rotating the through-wedge measurement model by 90° and designing it to integrate with the optical path. Across-wedge spectra were acquired at 3.25, 5.75 and 8.25 mm away from the model top, as annotated in Figure 2. As VUV radiation can be absorbed by ambient molecular oxygen, the optical path has to be enclosed and evacuated to low vacuum to the level of 10^{-2} Pa. To enable the measurements depicted in Figure 2, precise vertical adjustment of the optical path was imperative to shift its axis to various locations above the model top, which was realised through the design of an adjustable side flange for test section. Linear bearings were installed underneath the legs of the optics table to facilitate smooth horizontal translation.

On account of operation cost and structural integrity of the light tube, the diameter of the magnesium fluoride window was opted to be 25 mm. With margins left for attachment to the window holder and sealing of the entire optical path, the effective diameter of the window is 21 mm. To image this length of flow onto the slit, and ultimately the imaging sensor with a length of 6.9 mm along the spatial axis of the spectrum, a magnification of 0.32 was calculated. However, to reserve some spatial margins and with the edge of the image intensifier being circular, a magnification of 0.2 was adopted.

Fully enclosed in the optics box, as shown in Figure 4, the external optics comprised of a flat mirror and a f=500 mm concave mirror with an aperture plate mounted in front of it. These mirrors were coated with aluminium and magnesium fluoride for optimised reflectance in the 120 to 200 nm wavelength region. The focal plane contained the nozzle centreline, and the image plane lay roughly at the spectrometer entrance slit. With the thin lens formula, the positions of the mirrors could be worked out. The combined distance between nozzle centreline and the flat mirror plus that between the two mirrors was 3000 ± 10 mm. The distance between the concave mirror and the spectrometer entrance slit was 600 ± 5 mm. An aperture diameter of 30 mm was chosen to achieve a theoretical depth of field of 100 mm with a circle of confusion diameter of 0.1 mm and to ensure that the spectrometer was not over-filled.

The spectral image acquired by the ICCD camera is a two-dimensional 2048×512 array of 16-bit integers. The length of the image is aligned with the wavelength axis, and the width of the image is parallel to the spatial axis. To convert pixel counts into physical quantities characterising the radiation emitted from the high temperature plasma, the relationship between the pixel counts and actual physical quantity needs to be established. Pixel location contains information regarding wavelength and position depending on its index

values along the spectral and spatial axes of the image array. The calibration is therefore composed of radiance, wavelength, and spatial calibration.

The source used in the radiance calibration was the McPherson^{TM} model 632 deuterium (D_2) lamp calibrated by Physikalisch-Technische Bundesanstalt.[15] The lamp had a MgF_2 front window and a beam circular of F/7. The emitting element of the lamp had a diameter of 1 mm and was situated 81 mm behind the front surface. As the end of the light tube was designed with a sliding seal and allows length adjustment up to about 90 mm, the emitting element of the lamp could be placed exactly on the nozzle centreline. The D_2 lamp was calibrated from 116 to 410 nm, and the spectral radiance of the lamp was measured for circular areas of 0.60, 0.92 and 1.01 mm diameters. The measurement had a spectral bandwidth of 0.8 nm full width at half maximum (FWHM) between 116 and 172 nm, and 1.6 nm from 172 to 410 nm.[15] The relative uncertainty of the deuterium lamp spectral radiance is given in Table 5.

Table 5. Relative uncertainty of the deuterium lamp spectral radiance

Spectral Range	Spectral Bandwidth	Relative Expanded Uncertainty (k=2)
116.0 - 120.4 nm	0.8 nm	14%
120.6 - 122.6 nm	0.8 nm	36%
122.8 - 170.0 nm	0.8 nm	14%
172 - 410 nm	1.6 nm	7%

Radiance calibration is based on the principle that the system sensitivity was the same during the calibration and the experiments, which is the ratio of pixel counts per unit time to the spectral irradiance $E(\lambda)$ of incident radiation. System sensitivity $S(\lambda)$ is a function of wavelength, and is determined by the performance and characteristics of the optical configuration and individual components. Due to the in situ nature of the calibration, the solid angle of the radiation captured by the optics is the same, and the system sensitivity can be therefore denoted as counts per unit time per unit spectral radiance $I_e(\lambda)$ of collected radiation as below:

$$S(\lambda) = \frac{C_p}{t_e I_e(\lambda)} \tag{1}$$

In the equation, C_p is the number of counts recorded on each pixel, and t_e is the exposure time. With the radiance of the D_2 lamp orders of magnitude lower than that of the high-temperature plasma generated around the test model, a much longer exposure time had to be used in the calibration. The camera reciprocity or linearity of pixel counts with exposure time is therefore critically important to ensure the validity of Equation 1. The reciprocity of the camera was measured from 0.25 to 200 µs, between which good linearity was observed.

The evaluation of the system sensitivity was not so straightforward as described in Equation 1 and a two-step approach is adopted. In the first step, a baseline VUV spectrum of the deuterium lamp was acquired. The lamp was attached to the end of the light path via an adapter, and the light tube length was adjusted so that the radiating element of the lamp lay on the nozzle centreline. When the pressure of the optical path was below 10^{-2} Pa, the light path height was adjusted via the test section side plate that it's attached to. The procedure was conducted to improve the alignment of the D_2 lamp with the existing optics that was aligned with the test model. This procedure was made necessary because of the small diameter of the deuterium lamp emitting element. Without refined alignment, the diameter of the image wouldn't fall on the spectrometer entrance slit. This could lead to deviation from the official calibration data and ultimately erroneous system sensitivity.

For the across-surface measurements, the baseline system sensitivity in the VUV range was independently carried out for measurements at 3.25, 5,75 and 8.25 mm above wedge top. Between these experiments, the optics table was both horizontally and vertically shifted, and a new MgF_2 window was used for each shot as mentioned earlier. The comparison between these baseline system sensitivity measurements is presented in Figure 5. The deviations between the results are within the uncertainties of the deuterium lamp calibration, and lends confidence to the optics alignment between measurements at varied locations, as well as the

consistency of the MgF_2 windows' transmittance.

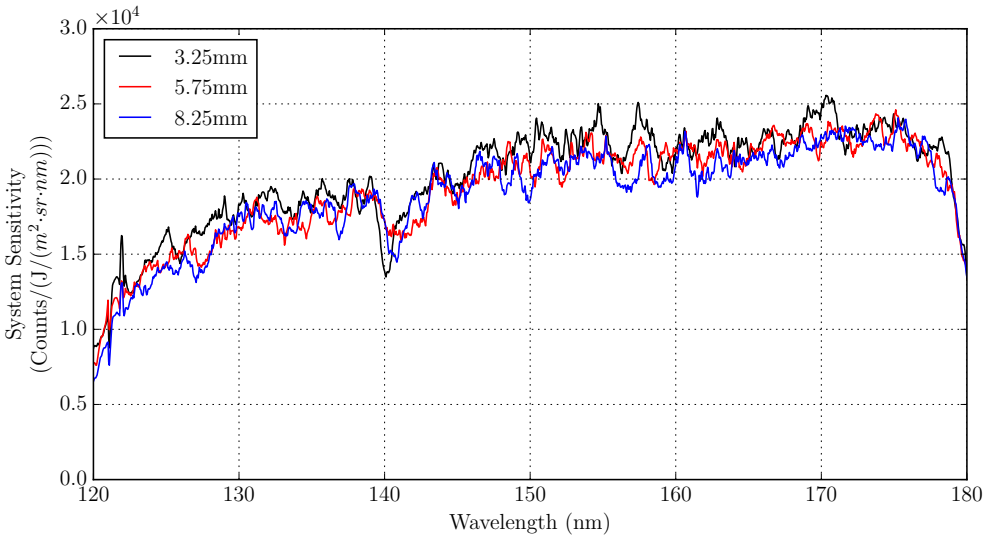

Figure 5. Baseline system sensitivity at 3.25, 5,75 and 8.25 mm above wedge top

Due to the astigmatism of the optical system in the direction vertical to the length of the spectrometer entrance slit and limited uniformity of the deuterium lamp output, a conversion factor had to be obtained and applied to the baseline system sensitivity acquired in the previous step. This was done by comparing the ultraviolet (UV) spectra of the deuterium lamp and an integrating sphere between 350 and 400 nm. The integrating sphere was custom-made by Labsphere®, and was calibrated from 300 nm to 1.0 µm with an interval of 10 nm. 350 to 400 nm was the ideal range to compare the two calibration sources in that the absolute difference between the spectral radiance of each source are small, which ensured more accurate characterisation of the entire range with the given dynamic range and signal-to-noise ratio performance of the ICCD camera. The more important reason for selecting this range had to do with the characteristics of the deuterium lamp output.

The spectral radiance of the D_2 lamp in the 116 to 200 nm VUV range is two orders of magnitude higher than that in the 300 to 410 nm UV range which overlaps with the integrating sphere output. Considering the second- and third-order effects of the spectrometer grating, special procedures were taken. The output of the deuterium lamp plunges from 162 nm until it drops by an order of magnitude at 170 nm. Consequently, the second- or third-order effects of VUV radiation between 150 and 175 nm on the 300 to 350 nm region is much higher than its 175 to 200 nm counterpart on the 350 to 400 nm. Although it's possible to insert a UV long pass filter into the optical path to block the VUV components of the deuterium lamp output, it was infeasible due to the spatial constraints of the optics chamber until a new adapter was designed after the experimental campaign.

The second step of the calibration started right after the baseline VUV spectrum of the deuterium lamp was acquired. The grating was adjusted to the central wavelength of 375 nm. The pumping system was deactivated and the vent was briefly opened to introduce a small amount of air into the optical path. Water vapour and molecular oxygen in air absorbs in the VUV of the D_2 lamp output and eliminates the second and third-order effects. The pressure at which the optical path was vented to needed to be determined experimentally because substantial pressure change might alter the deformation of the optics box and change the characteristics of the optics configuration. Repeated tests have been done to acquire the UV spectrum of the deuterium lamp under different light path pressures. Direct comparison of UV spectra of the deuterium lamp from 0.02 to 1500 Pa is exhibited in Figure 6.

According to Figure 6, the pixel counts at all wavelengths decrease with increasing pressure until the optical path pressure is vented to above 500 Pa. A strong peak can be observed at about 365 nm, which is believed to be the third-order of the extremely strong 121.534 nm Lyman-α peak. It disappears as the optical path is vented to above 10 Pa. To better characterise the influence of pressure on the UV spectrum of the deuterium lamp, system sensitivity in the UV range is calculated based on the spectra at various

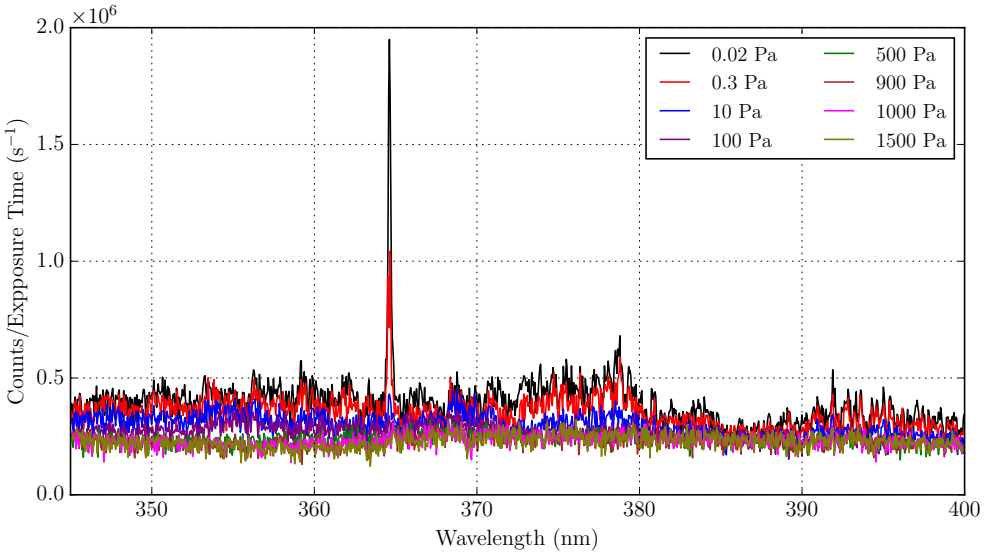

Figure 6. UV spectra of the deuterium lamp at different optical path pressure levels

pressure levels and is presented in Figure 7.

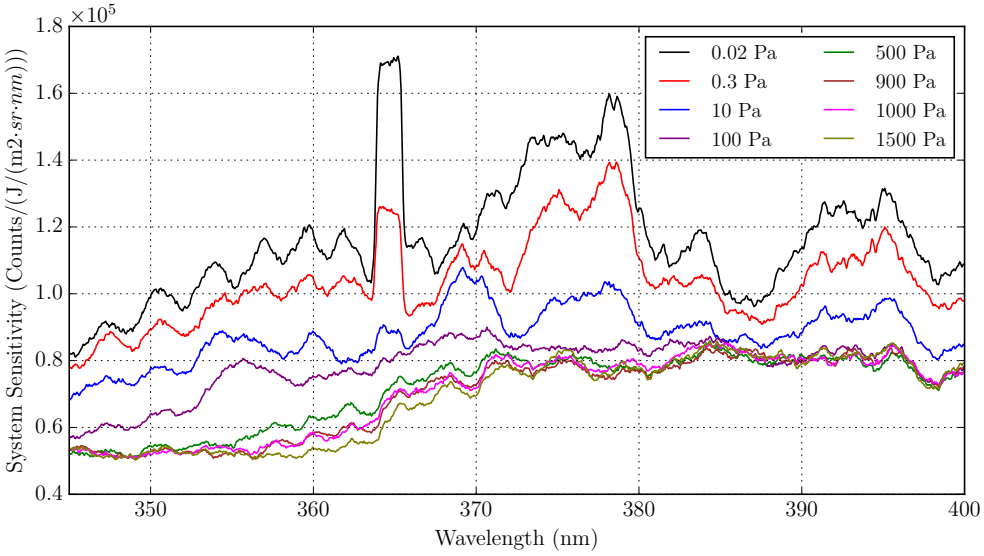

Figure 7. System sensitivity in the UV range evaluated with deuterium lamp spectra acquired at different optical path pressures

When evaluating system sensitivity, D_2 lamp spectra were spectrally averaged to account for the lower spectral resolution reported in the UV range in the calibration certificate.[15] As a result, the peak in Figure 6 appears rounded and makes the differences due to varied pressure values more distinguishable. It's observed that once the pressure is above 500 Pa, the calculated system sensitivity becomes stabilised between 345 and 355 nm, and that at longer wavelengths gradually asymptotes to the value in this wavelength range as the pressure increases. In the 350 to 400 nm wavelength range, the transmittance of the MgF_2 window, the reflectance of the mirrors and the grating, as well as the quantum efficiency of the ICCD camera are quite uniform. Consequently, the system sensitivity is expected to be fairly constant in this wavelength region. This leads to the conclusion that at 1 kPa, the second- and third-order effects on the D_2 lamp UV spectrum

from 345 to 355 nm is negligible. Therefore, direct comparison can be made in this spectral range between system sensitivities evaluated with the integrating sphere and the deuterium lamp, which is exhibited in Figure 8.

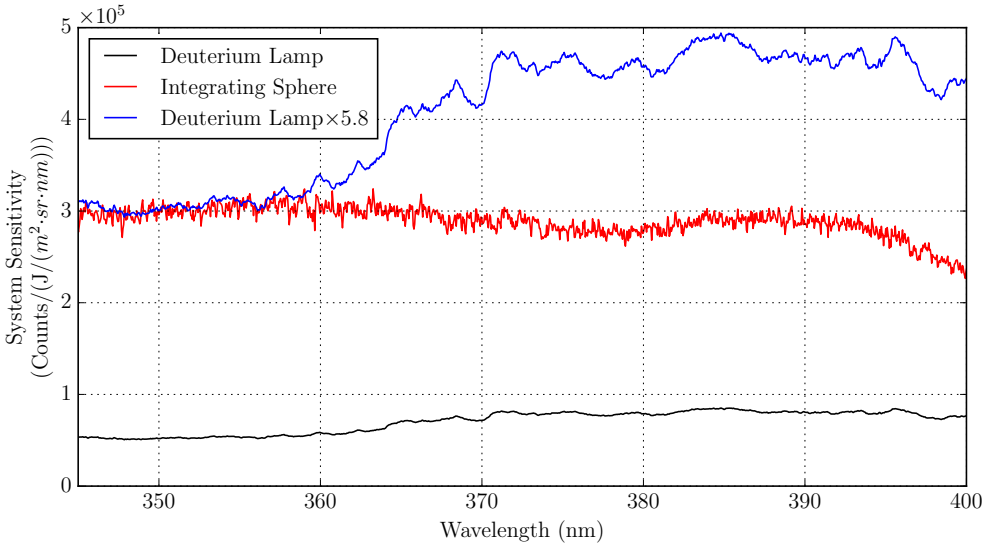

Figure 8. The comparison between system sensitivity evaluated using the spectra of the deuterium lamp and the integrating sphere

A factor of 5.8 was found between the two, which was the same for independent calibrations done for across-surface measurements done at 3.25, 5.75 and 8.25 mm above model top. This baseline VUV system sensitivity is multiplied by this factor to obtain the final system sensitivity. The conversion from pixel count to spectral radiance was done with Equation 1 by substituting the counts and exposure time with the experimental values.

Wavelength calibration was performed to establish the relationship between pixel column number and wavelength values. It was carried out for spectra acquired in the experiments in VUV and radiance calibrations done both in the VUV and UV range. For the baseline VUV calibration, strong peaks of the deuterium lamp output were made use of, which were the 121.534 nm Lyman-α peak and the 161.0 nm line. For the second-step in radiance calibration, wavelength calibration in the UV range was conducted with the help of a pencil style mercury argon lamp 6035 manufactured by Newport®. The peaks were the 365.0153, 365.4836 and 366.3279 nm mercury lines.

As grating rotation was unavoidable between alignment, calibration and experiment, the exact wavelength value associated with each pixel on the CCD sensor might vary. For this reason, wavelength calibration was independently carried out for each spectral image acquired in the experiments. The peaks used were the strong 141.194, 149.2625 and 174.2729 nm atomic nitrogen lines. Once the peaks were identified, a linear regression was performed to associate pixel column number with wavelength values. With more than 30 wavelength calibrations done for all the shots, the relative deviation in the relative peak pixel column number was 1. The uncertainty in wavelength calibration was therefore within 1 pixel, or 0.05 nm.

During the alignment of the optics, aluminium plates with equally spaced holes were vertically mounted on both sides of the wedge model. The image acquired by the camera could be used to infer the relationship between pixel row number and distance, which was 0.109 mm/pixel. Combined with the actual size of a pixel, which is 13.5 µm in length, the actual magnification turned out to be 0.205.

The spectral line shape measured by the emission spectroscopy system is a convolution of the actual line shape and the instrument function, which describes the intensity distribution of output from a monochromatic input.[16] Optical aberrations, finite slit width and grating imperfections can contribute significantly to the broadening of spectral lines. The instrument function can be measured by acquiring an image of an integrating sphere placed at the focal plane with the grating rotated to its zeroth order position. With $\Delta\lambda$ being the distance from the line centre, and λ_G and λ_L the half width at half maximum (HWHM) for the

Gaussian and Lorentz components separately, the instrument function takes form of a Voigt profile below:

$$
\begin{aligned}
G(\Delta\lambda;\lambda_G) &= \sqrt{\frac{ln2}{\lambda_G^2\pi}} exp(-ln2(\frac{\Delta\lambda}{\lambda_G})^2) \\
L(\Delta\lambda;\lambda_L) &= \frac{1}{\pi}\frac{\lambda_L}{\Delta\lambda^2+\lambda_L^2} \\
V(\Delta\lambda;\lambda_G,\lambda_L) &= \int_{-\infty}^{\infty} L(\Delta\lambda;\lambda_L)G(\Delta\lambda-w;\lambda_G)dw
\end{aligned}
\tag{2}
$$

The fit is presented in Figure 9. The corresponding parameters are $\lambda_G = 0.0479$ nm and $\lambda_L = 0.0588$ nm.

An edge measurement was made during the experiment to account for the spatial resolution of the ICCD camera.[17] A sharp edge was placed on the focal plane and was illuminated by a fluorescent lamp. An image was acquired with the grating rotated to its zeroth order. Spatial derivatives of camera counts across the image of the sharp edge along the zeroth order line-centre were fitted to Voigt profiles to characterise the spatial resolution of the CCD sensor. Such spectral images have been acquired with the knife edge placed on the nozzle centreline, as well as on each side of the wedge model, which were denoted as the far or near side based on the distance from the optics. One of the resulting profiles is presented in Figures 10 for measurement at nozzle centreline. Fitted HWHM values of the Gaussian and Lorentz components for each measurement are tabulated in Table 6.

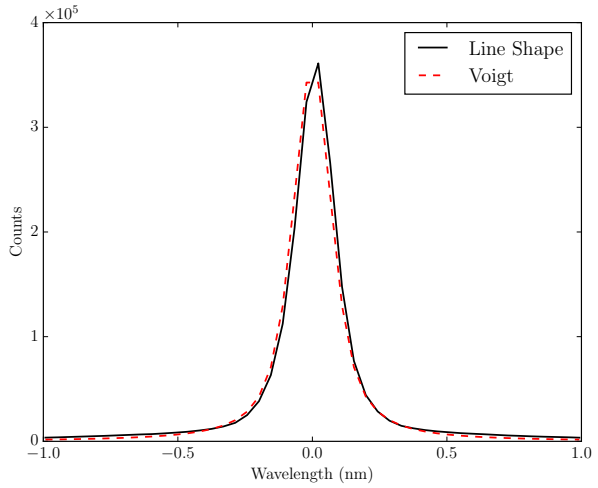

Figure 9. Voigt fit of the zeroth order spectral line shape

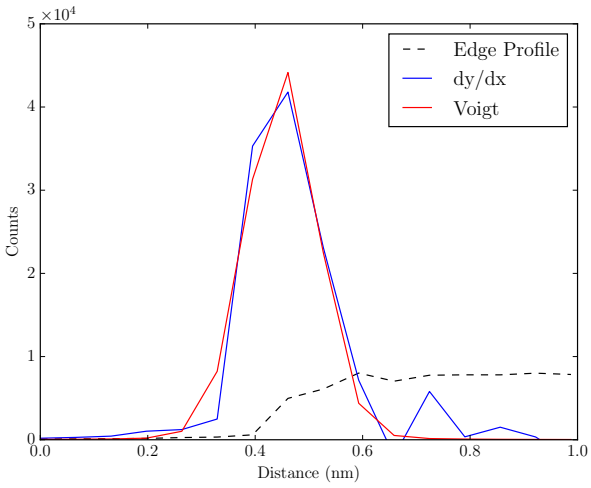

Figure 10. Camera resolution function fitted to a Voigt profile for knife edge placed on nozzle centreline

Table 6. Gaussian and Lorentz HWHM of the fitted Voigt profiles for the camera resolution measurements

Knife Edge Position	Centre	Near	Far
Gaussian HWHM (mm)	0.0750	3.0×10^{-6}	1.6×10^{-4}
Lorentz HWHM (mm)	0.0036	0.0503	0.0105

E. Filtered Imaging

In the experiments, a 1 MHz Shimadzu® HPV-1 high speed camera was set up on the other side of the test section to acquire luminosity images. A Nikon AF Micro-Nikkor AF 200mm f/4D IF-ED lens was attached to the camera. With the flow strongly radiating in the near infrared (NIR) region, a Thorlabs FBH780-10 band-pass filter was coupled to the camera lens to record two-dimensional images of atomic nitrogen and

oxygen radiation. The filter had a central wavelength of 780 nm and a FWHM of 10 nm. The layout of the filtered imaging system is illustrated on the left of Figure 4.

An in situ calibration of the filtered imaging system was performed with the integrating sphere introduced in Section D. The principle of calibration is essentially the same as that of the VUV spectroscopy system calibration. The radiance level represented as pixel counts is the radiance transmitted through the filter and weighted by the high speed camera spectral response. As the average transmittance of the FBH780-10 filter between 776.5 and 778.0 nm is 87.8% with a standard deviation of 1.06%, coupled with the fact that the 777 nm oxygen triplet is the predominant line in the narrow wavelength region, the total radiance of the oxygen triplet can be directly calculated by assuming a constant camera spectral response between 760 and 800nm, which happens to be the case according to the quantum efficiency curve provided by the manufacture. The added relative error due to this simplification is within 2%.

Unlike contemporary ICCD cameras with up to 16-bit dynamic range , the Shimadzu® HPV-1 high speed camera has a dynamic range of only 10-bit. When using the camera for calibration, not a single image but a stack of 102 images were acquired. To extract the mean counts of the image of the integrating sphere, a square region of 75×75 pixels was selected and is shown in Figure 11. A number of dark spots can be observed, which were produced by defective pixels that read out significantly lower-than-average or even zero counts. To pinpoint and exclude these defective pixels, a histogram of the image is made and can be found in Figure 12. Apart from the faulty pixels detected, counts of the functioning pixels were found to be distributed in a pattern similar to that of a normal distribution with a mean of about 225. The average count was obtained from pixels that produce counts above the cut-off limit of 200.

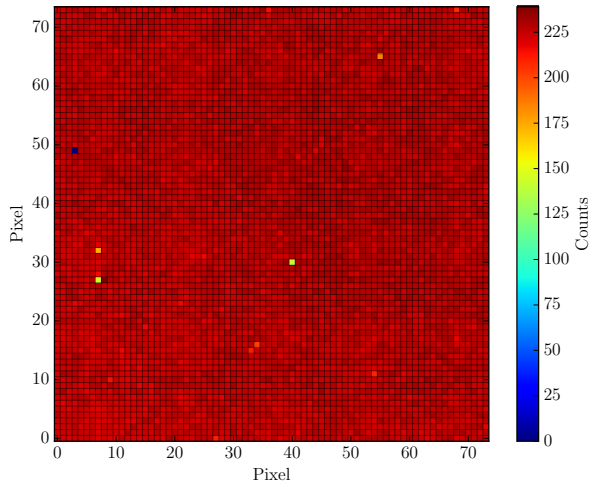

Figure 11. Selected 75×75 pixels region of the integrating sphere image with visible pixel grid

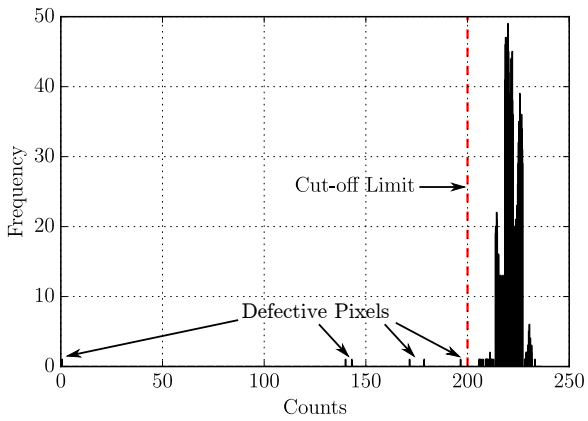

Figure 12. Histogram of the integrating sphere image selection

III. Numerical Simulations

Simulations were performed using Eilmer3, a finite-volume Navier-Stokes flow solver[18] implemented on block-structured grids developed at the Centre for Hypersonics. The computational domain starts as a narrow region enveloping the leading edge of the wedge, gradually expands to cover the oblique forebody shock wave and then turns 90° at the wedge corner. Such a geometry necessitates a large number of blocks to produces cells with low deformity. Cell density assigned to the expansion fan is similar to that in the compression region behind the shock due to interest in the expanding flow and numerical challenges posed by rapid flow expansion.

Commercially available multi-block structured grid generator GridPro®[19] was employed, and the same block topology was applied to Conditions 2 and 3 with the inflow boundary varied to account for differences in shock stand-off distances. A slightly different topology was adopted for Condition 1 given the smaller shock angle. The 320-block grid topology and boundary conditions are shown in Figure 13. Local grid refinement was applied near the wedge surface to resolve the boundary layer, and more cells were packed

near the shock wave to improve resolution of large gradients of flow variables.

The computational domain was defined by the inflow boundary, walls of the wedge model comprising the leading edge, the corner and shoulder, and the upper and downstream outflow boundaries. The inflow parameters were obtained from the experimentally averaged flow conditions described in Section B. The wedge wall was set to a fixed room temperature of 298.15 K. Due to the short test time prior to spectrum acquisition (< 60 µs), large size of the model, and good thermal conductivity of the material (stainless steel), the wall temperature rise is considered to be negligible and so is its influence on the flow field. The flow was assumed to be laminar for all three conditions based on the inflow Reynolds numbers calculated based on the width of the wedge, which were below 20 000. At the outflow boundary, the cell data on the outside were extrapolated from neighbouring ones inside the computational domain.

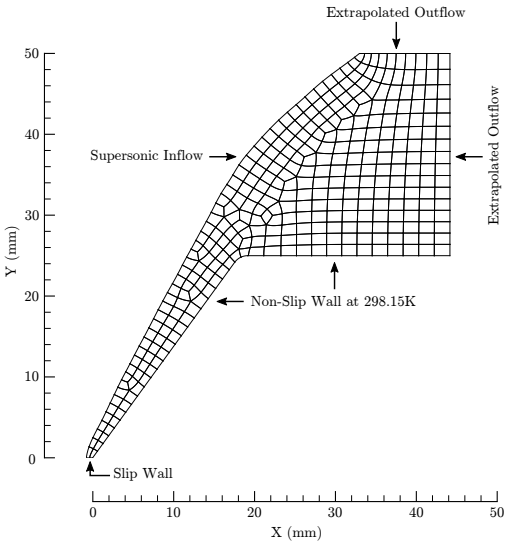

Figure 13. Schematic of the block topology and boundary conditions

A mesh independence study was conducted with cell numbers of 196 299, 226 213 and 274 594. Atomic nitrogen number density along a line of sight 3.25 mm above the wedge top was compared between simulations on different grids, and is presented in Figure 14. N number density is sensitive to flow density changes and chemical reactions, and the excellent agreement between the simulations with different mesh densities demonstrates that 196 299 cells are sufficient.

A two-temperature gas model was adopted in the simulations with 11 species included: N, N^+, NO, NO^+, N_2, $N_2{}^+$, O, O^+, O_2, $O_2{}^+$ and e^-. The heavy-particle (both molecules and atoms) translational temperature was assumed to be in equilibrium with molecular rotational temperature and the molecular vibrational temperature equilibrates with the electron translational as well as electronic excitation temperatures.[20] The translational-rotational temperature is denoted as T_{tr}, and T_{ve} is used to represent vibrational, electron-translational and electronic temperature. The thermo-chemical models used in this work were implemented by Gollan[21] and Potter.[22]

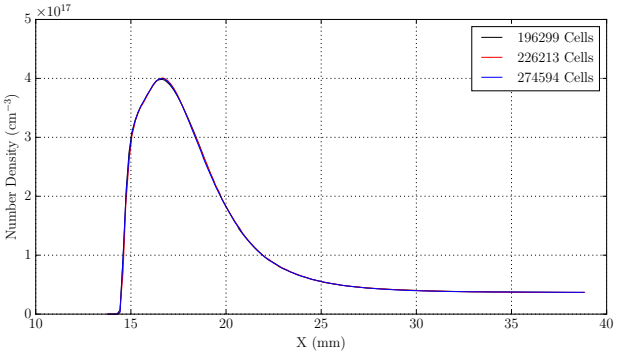

Figure 14. Atomic nitrogen number density at 3.25 mm above wedge top for simulations with various cell numbers

The flow was modelled as a mixture of thermally perfect gases, and each thermal mode was assumed to be populated by a Boltzmann distribution dictated by the associated temperature.[22] Transport properties were obtained with the Gupta-Yos mixing rules[23] and collisional integrals from Wright.[24,25] Chemical reaction scheme and rate coefficients were from Park,[26] in which the reaction rates were governed by a single rate-controlling temperature defined as $T_d = \sqrt{T_{tr}T_{ve}}$. A different temperature expression of $T_d = T_{tr}^{0.7}T_{ve}^{0.3}$ was used here which was found to achieve better agreement with the SSH theory.[27,28] Vibrational-translational energy exchange was calculated using the Millikan and White[29] correlation with Park's high temperature correction.[26] Electronic-translational energy relaxation was modelled with the equation proposed by Appleton and Bray.[30]

The radiation modelling was carried out in an uncoupled fashion by feeding steady-state flow variables along different lines of sight to the radiation modelling code, which was NEQAIR v14[31] in this work. Radiation transport calculations were done along these lines of sight and radiance perpendicular to them were output by running NEQAIR in *shock tube mode*. The tangent-slab approximation was made in the calculation. Associated atomic and molecular spectral systems were activated for species present in the flow, and the non-Boltzmann model was opted for calculating the number densities of excited states. The wavelength range covered by the simulation spanned from VUV at 85 nm to NIR 2.5 µm. The spectral range was

subdivided into VUV, UV, VIS and NIR to evaluate the contributions of each wavelength segment to the total radiative heating. To facilitate comparisons with experimental data, separate NEQAIR simulations were run with the addition of narrow wavelength sections to output the total radiance of individual spectral lines. Instrument functions fitted in Section D were applied to the simulated spectra.

The three flow conditions were compared with each other in the flow properties behind the oblique shock and into the afterbody. As mentioned in Section B, flow parameters for each condition were obtained by averaging those from a selection of experiments with minimum shot-to-shot variations. Although the best practice is to run a simulation for each experiment and compare the results accordingly, it was not feasible due to the limited computational resources. A compromise was made by simulating each flow condition with the experimentally averaged values so that comparisons could be made between the simulation and experimental data at the same condition. Inflow parameters for all three conditions were presented in Table 7, with thermochemical equilibrium assumed.

Table 7. Inflow parameters for Conditions 1, 2 and 3

Condition	1	2	3
Static Pressure (Pa)	1308	1520	843
Temperature (k)	2609	2713	2892
Velocity (m/s)	9714	10899	11837

Flow temperature and velocity increases from Conditions 1 to 3. Pressure is the highest at Condition 2, and the lowest at Condition 3. Equilibrium species mole fractions are presented in Table 8. The dominant species for all three inflow conditions are N_2, O_2, O and NO. For O_2, the degree of dissociation increases with temperature, which is 26%, 34% and 64% for Conditions 1, 2 and 3 respectively. The level of dissociation for N_2 follows the same trend, although the dissociated N_2 is less than 1% for all three conditions. Due to the relatively moderate inflow temperatures, the flow is barely ionised. NO^+ is the predominant ion, with a mole fraction orders of magnitude higher than other ions. The mole fraction of free electrons is also very low as a result.

Table 8. Equilibrium inflow mole fractions for Conditions 1, 2 and 3

Condition	1	2	3
N	5.82×10^{-6}	1.25×10^{-5}	6.13×10^{-5}
N^+	/	2.04×10^{-20}	2.12×10^{-18}
NO	2.27×10^{-2}	2.47×10^{-2}	2.21×10^{-2}
NO^+	1.00×10^{-8}	2.23×10^{-8}	1.04×10^{-7}
N_2	7.46×10^{-1}	7.34×10^{-1}	6.93×10^{-1}
N_2^+	2.33×10^{-18}	1.39×10^{-17}	3.69×10^{-16}
O	8.19×10^{-2}	1.12×10^{-1}	2.18×10^{-1}
O^+	3.35×10^{-16}	1.97×10^{-15}	6.37×10^{-14}
O_2	1.49×10^{-1}	1.30×10^{-1}	6.73×10^{-2}
O_2^+	1.21×10^{-12}	3.49×10^{-12}	1.98×10^{-11}
e^-	1.00×10^{-8}	2.23×10^{-8}	1.04×10^{-7}

IV. Results and Analysis

A. Flow Establishment

The data acquisition system was activated by a trigger box, which was triggered by the output from a photodiode pointed to the leading edge of the model. The acquisition of VUV spectrum was completed over a duration of 0.16 to 6 µs, depending on the flow condition and configuration of the measurement, i.e.,

across- or through-surface measurements. Time-resolved measurements were necessary to provide evidence of flow steadiness over the period wherein the spectral measurement was made. Pressure trace from the PCB® 112A22 transducer housed in a 15° half-angle cone assembly underneath the model can be used to indicate steady test time. It should be noted that a finite time is required to establish the flow around the cone and fill the plenum, which is roughly estimated to be about 10 µs for the three flow conditions. The lag or response time of the pressure signal to the actual inflow is therefore expected to be of a similar magnitude. The high speed camera is a better alternative as it gives a time resolution of 2 µs when operated at a frame rate of 5×10^5fps.

Data from the pressure transducer mounted under the model and the gating output of the ICCD camera were acquired together with the signals from the multiple wall-mounted pressure sensors along the facility. Figure 15 shows the window of spectral image acquisition, pressure transducer trace and high speed imaging frame coverage. Also presented in the plot are the traces of the photodiode signal and that of the trigger box output. The time axis is aligned with the first frame of the high speed footage. The high speed camera was configured to record 10 frames or 20 µs prior to receiving trigger signal from the trigger box.

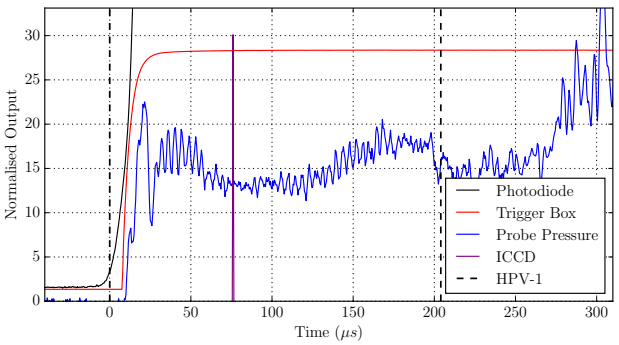

Figure 15. Normalised trace of the under-model pressure transducer, trigger signals and gating outputs of the Andor® ICCD camera and Shimadzu® HPV-1 high speed camera for shot x2s3022 with Condition 3

A steady test flow duration of 70 µs can be inferred from the pressure trace, which starts roughly 20 µs prior to the acquisition of the VUV spectrum. Considering the lag in the response of the pressure transducer to incoming flow, the actual starting point of the steady test time can be more than 30 µs earlier than the triggering of the ICCD camera. To combine visual evidence with the pressure trace, six representative frames of the high speed images are inserted in Figure 16. These images were acquired with a Thorlabs® FBH-780 filter coupled to the high speed camera, and are representations of the development of 777 nm atomic oxygen triplet. Flow arrival is first captured by the high speed camera at Frame 9, or T=18 µs relative to the first frame. It takes roughly 30 µs for the forebody shock layer to stabilise, and another 16 µs or so to establish the steady expansion fan and afterbody flow. After about a further 8 µs, the upper edge of the shock layer becomes unstable and begins to oscillate, and pixel counts in the shock layer are also found to decrease. Similar trends were also observed for Conditions 1 and 2.

To quantitatively examine the flow steadiness during the test window, raw counts along certain rows of pixels corresponding to different distances above the top of the wedge are extracted from filtered high speed images. Spatial distributions of the pixel counts extracted from consecutive frames at 5.75 mm above the wedge are compared and presented in Figure 17. A steady test time of 8 µs can be found for Condition 3. The available test windows for Conditions 1 and 2 are obtained in the same fashion and are 8 and 6 µs respectively.

B. VUV Spectra

In every experiment, an image was acquired by the ICCD camera activated with a preset delay after receiving the trigger signal from the trigger box. The delay values were obtained based on analysis of the high speed images and considering the number of pre-trigger frames of the high speed camera, and were 54, 54 and 60 µs for the three flow conditions. Exposure time settings with different measurements were listed in Table 9. The exposure times for the through-wedge measurements were higher due to the smaller depth of the radiating flow.

1. Across-Wedge Spectra

The raw spectral image of shot x2s3022 with Condition 3 is presented in Figure 18. In the image, the test flow travels upwards along the spatial axis and individual spectral lines are spread along the spectral axis. Following the procedure described in Section D, the image can be calibrated with spectral radiance

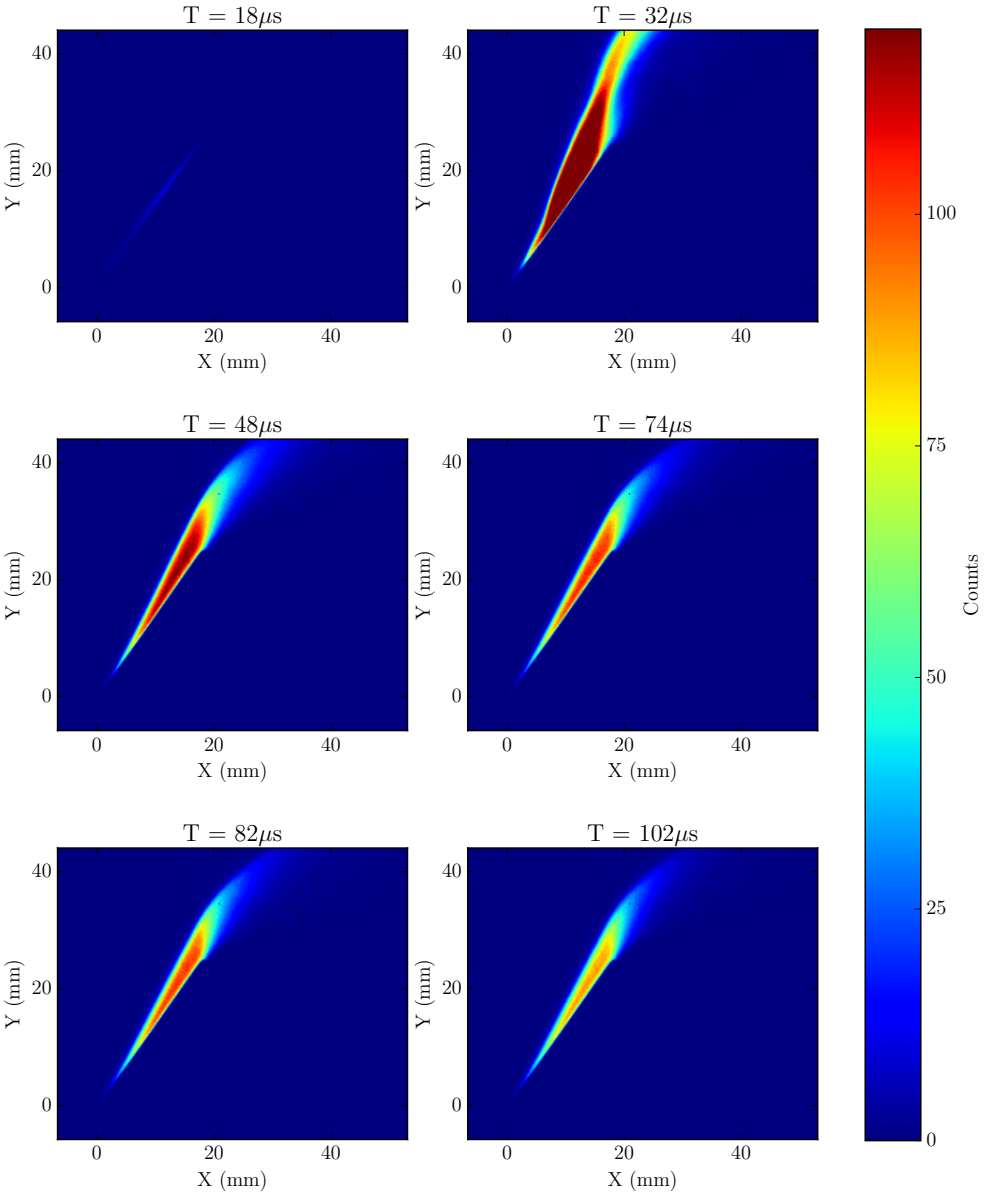

Figure 16. Representative high speed images of shot x2s3022

Table 9. Exposure time settings (μs) for the acquisition of VUV spectra

Measurement	Condition 1	Condition 2	Condition 3
3.25 mm above wedge	1.2	0.30	0.16
5.75 mm above wedge	1.6	0.40	0.20
8.25 mm above wedge	2.0	0.50	0.25
Through-wedge	6.0	2.0	1.0

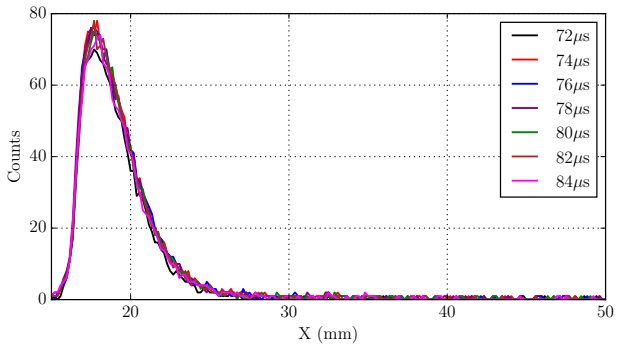

Figure 17. Pixel counts extracted at 5.75 mm above the top of the wedge from filtered high speed images of shot x2s3022

($W/(m^2 \cdot sr \cdot nm)$) values replacing the pixel counts, as shown in Figure 19. The wavelength extends from 118 to 180 nm, and a length of approximately 20 mm is effectively covered along the spatial axis. Associated rows of the image are integrated to yield a spatial profile of a spectral line's radiance ($W/(m^2 \cdot sr)$, such as the 149 nm N line shown in the upper right of the figure. The image has also been averaged over selected columns to obtain spatially-averaged spectra in the peak region and the expansion fan, which are compared in the lower left section of the figure.

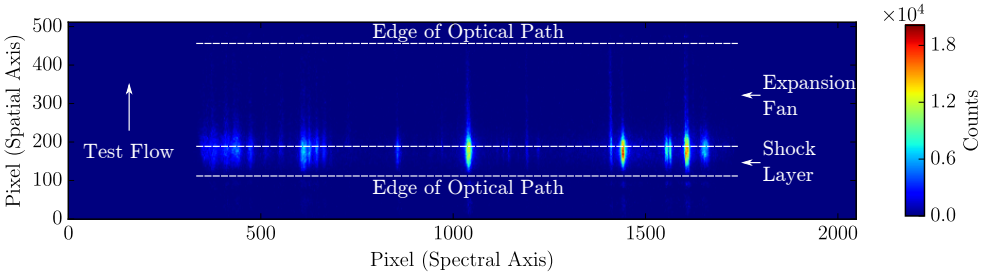

Figure 18. Unprocessed spectral image of shot x2s3022 with Condition 3 at 3.25 mm above the model

The National Institute of Standards (NIST) Atomic Spectra Database[32] was relied upon to identify various features of the spectra acquired. With N_2, O_2 and O dominating the flow exiting the nozzle, atomic nitrogen and oxygen are expected to dominate the VUV spectra due to strong post-shock dissociation and excitation. Also present in the spectra are spectral signatures indicative of impurities such as Al^+, C, Fe^+ and H. Shock layer spectra of the three flow conditions at 3.25 mm above the top of the wedge are exhibited in Figures 20 to 22, with prominent spectral features annotated with the associated radiators identified.

The level of contamination is generally found to increase with flow enthalpy. The most prominent contaminants are Al^+, C and Fe^+, which are of comparable radiance levels to the strong atomic nitrogen lines regardless of the flow condition. The Lyman-alpha line at 121.567 nm is the only outstanding hydrogen line, and can be observed for all three conditions. Al^+ most probably originates from the aluminium secondary diaphragm segregating the shock tube and the acceleration tube, and Fe^+ can come from the model and the tiny fragments of the primary diaphragm resting on the walls of the facility. With dry CO_2-free instrument air used to fill the shock tube, and test section as well as acceleration tube pressure evacuated below 20 Pa for all three conditions, C and H are less likely from CO_2 and H_2O in air than from hydrocarbon in vacuum grease applied at various stages of the facility.

Atomic nitrogen and oxygen lines identified in the spectra are tabulated in Table 10. Only two O lines are available in the table, as the 121.7648 nm O line is only vaguely observable in Condition 1 spectrum, barely visible for Condition 2, and is entirely dwarfed by neighbouring spectral lines for Condition 3. The 130.2168 and 130.4858 nm O lines are very close to each other, and partially overlap with adjacent N lines.

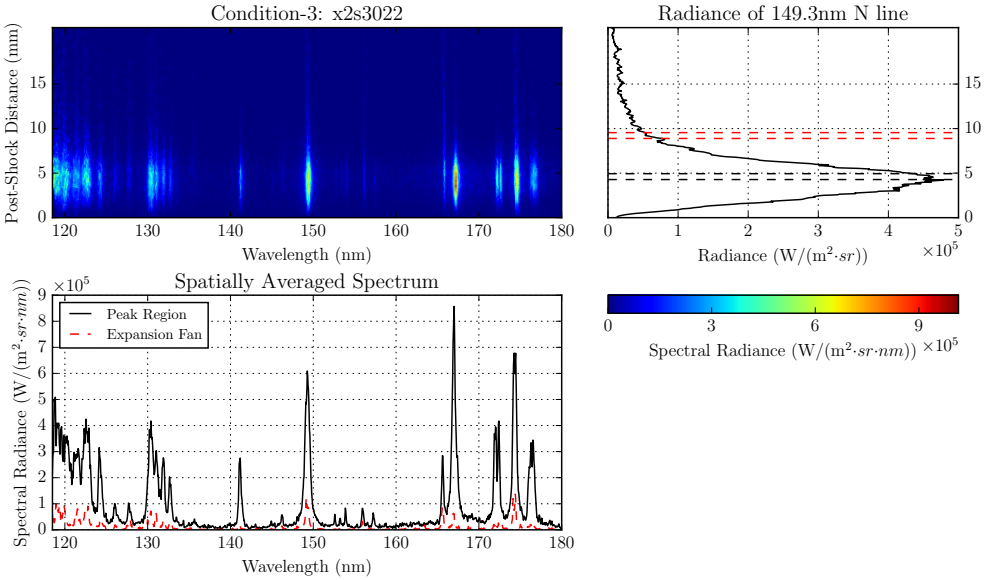

Figure 19. Calibrated spectral image of shot x2s3022 with Condition 3

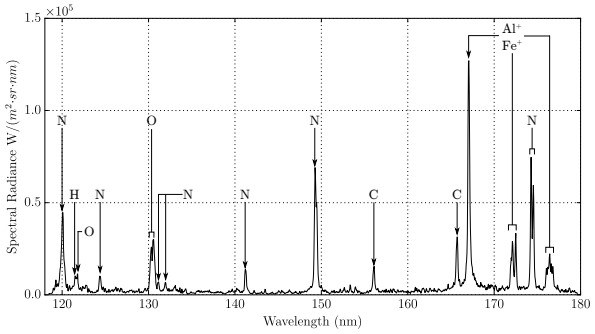

Figure 20. Radiator identification in the peak region spectrum of shot x2s3026 with Condition 1

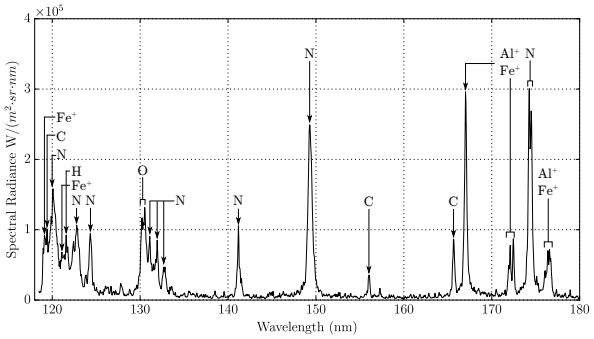

Figure 21. Radiator identification in the peak region spectrum of shot x2s3028 with Condition 2

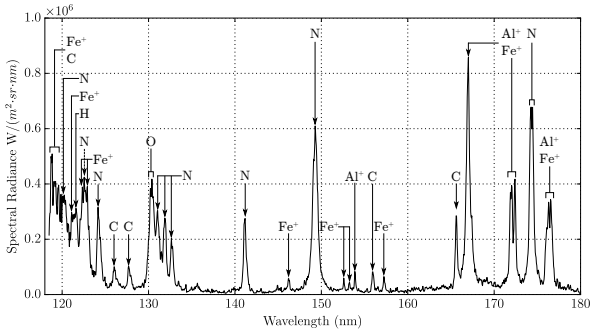

Figure 22. Radiator identification in the peak region spectrum of shot x2s3022 with Condition 3

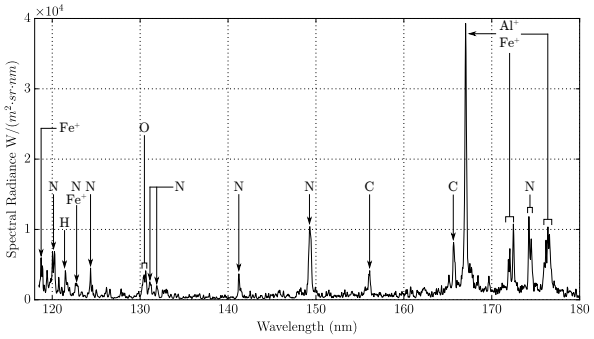

Figure 23. Radiator identification in the expansion fan spectrum of shot x2s3026 with Condition 1

Accordingly, most of the analysis and comparisons are made of atomic nitrogen lines above 140 nm. From Condition 1 to 3, nitrogen lines between 120 and 145 nm become increasingly stronger relative to their longer-wavelength counterparts, which can be attributed to higher shock layer temperatures.

Table 10. Wavelength of identified atomic nitrogen and oxygen lines

Wavelength (nm)	Radiator
120.0223 and 120.0710	N
122.537	N
124.3179	N
130.2168	O
130.4858	O
131.0540	N
131.900	N
132.657	N
141.194	N
149.2625 and 149.2820	N
174.2729	N
174.5252	N

Into the expansion fan, the species identified in the peak region spectrum continue to radiate, although at lower intensities. In contrast to shock layer spectra in Figures 20 to 22, some radiators become more prominent in the expansion fan spectra at 3.25 mm above the top of the wedge, presented in Figures 23 to 25 for conditions 1 to 3.

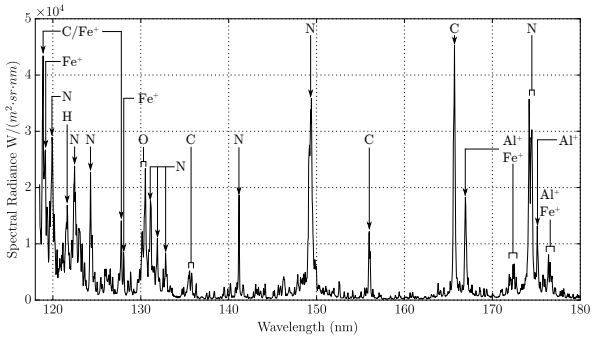

Figure 24. Radiator identification in the expansion fan spectrum of shot x2s3028 with Condition 2

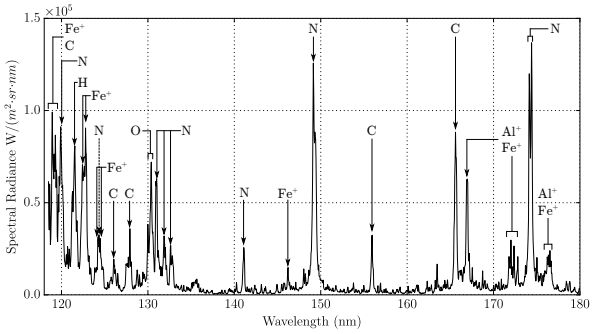

Figure 25. Radiator identification in the expansion fan spectrum of shot x2s3022 with Condition 3

For Condition 1, the 167 nm Al^+/Fe^+ line remains the strongest both in the peak region and in the expansion fan, however, it becomes relatively stronger compared to major N lines in the expansion fan. The relative strengths of other contaminant lines such as Fe^+ and C are also higher in the expansion fan. For Conditions 2 and 3, the relative importance of C lines increases in the expansion fan while that of the Al^+/Fe^+ lines between 160 and 180 nm declines. As the quantities of each contaminant fluctuates from shot to shot, the intensity of contaminant lines also varies. The general trends observed and summarised for each condition, however, are also observed for spectra at 5.25 and 8.75 mm above the top of the wedge.

Contamination in the flow has the potential of affecting the thermochemical process in the wedge flow due to the collisions between species in the test flow with intruding contaminants. The fragments of the secondary diaphragm, which is the major source of aluminium contamination in the flow, can also slow the flow down as a result of their existence. Care has been taken to clean the wedge model surface as well as the facility, yet the level of iron contamination remains largely unchanged. Proposals have been made to replace the steel shock tube with an aluminium one and this is hoped to reduce the level of iron contamination in the flow. The effectiveness of an oxygen plasma cleaner has been demonstrated at NASA Ames Research Center in reducing both hydrogen and carbon contamination.[33] Introducing such equipment could improve the quality of future experiments.

Contamination in the flow, although undesirable, may be of great value as carbon can be introduced into

the flow around a re-entry vehicle due to the ablation of carbon-based heat shield. As discussed above, the relative importance of carbon radiation tends to become stronger relative to major atomic N lines in the expanding flow for Conditions 2 and 3. By carefully introducing appropriate amounts of C into the CFD simulations to recreate the levels of radiation measured in the peak region, the spectrum of carbon lines in the expanding flow may be used to validate relevant carbon thermochemical models.

2. Through-Wedge Spectra

The through-surface spectra were acquired to reveal the contribution of each emitter to the radiative heat flux incident on the afterbody of the model, and to provide validation data for relevant computational models. As the through-wedge measurements were made along the line of sight parallel to the nozzle centreline, the results should be less susceptible to 3D flow effects and radial distribution of flow properties compared with the across-wedge measurements. Through-wedge spectra for Conditions 1, 2 and 3 are presented in Figures 26, 27 and 28 respectively.

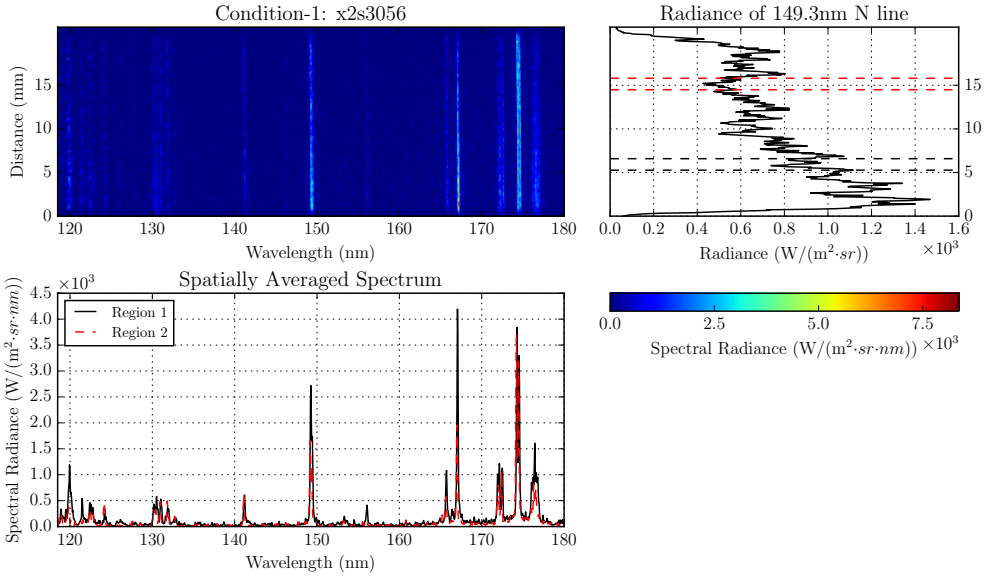

Figure 26. Through-wedge spectrum of Shot x2s3056 with Condition 1

A common feature shared by the through-surface spectra for all three conditions is that the radiance levels of most, if not all N and O lines are about an order of magnitude lower than the across-surface spectra under the same conditions. This could result from the much smaller depth of radiating flow through which spectra were acquired. In addition, low temperature flow close to the wall could give rise to the production of oxygen molecules via recombination reactions, which strongly absorb VUV radiation and reduce its level incident on model surface.

In contrast to across-wedge spectra, the through-wedge spectra for all conditions are less plagued by contaminants. The 167nm Al^+ line is the most if not the only prominent contaminant line for each condition. The 165nm carbon line is only noticeable in the very upstream region near the corner of the wedge, and the radiance levels of Al^+ and Fe^+ lines between 170 and 180nm are much weaker compared with the across-wedge spectra. This could indicate that larger proportions of the radiation from the contaminants are absorbed near the surface.

C. Comparisons between VUV Spectra and NEQAIR Simulations

1. Condition 1

Figures 29 and 30 exhibit the spatial profile comparison of 149 nm and 174 nm N lines between experiments and the simulations using NEQAIR. The most remarkable disagreement is the span of the profiles, with the experiment profiles extending more than twice the distance than those for the simulations. Such difference

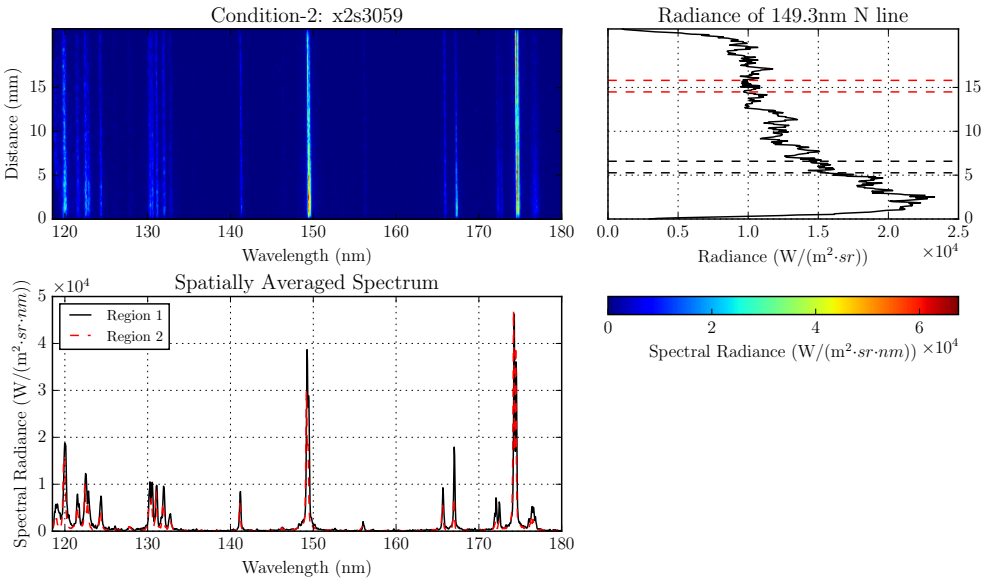

Figure 27. Through-wedge spectrum of Shot x2s3059 with Condition 2

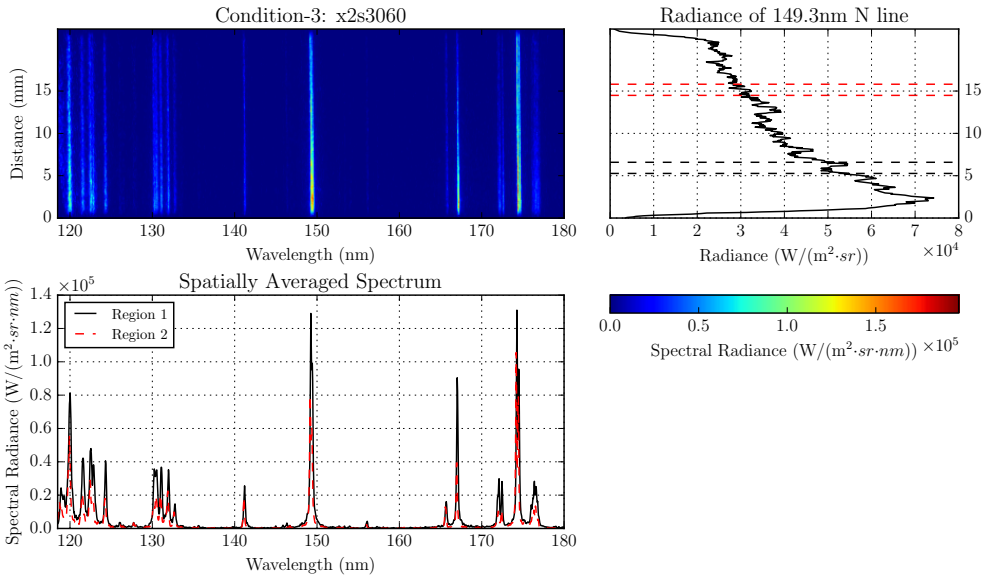

Figure 28. Through-wedge spectrum of Shot x2s3060 with Condition 3

translates into much higher integrated radiative heat flux incident over the afterbody surface than the NEQAIR prediction.

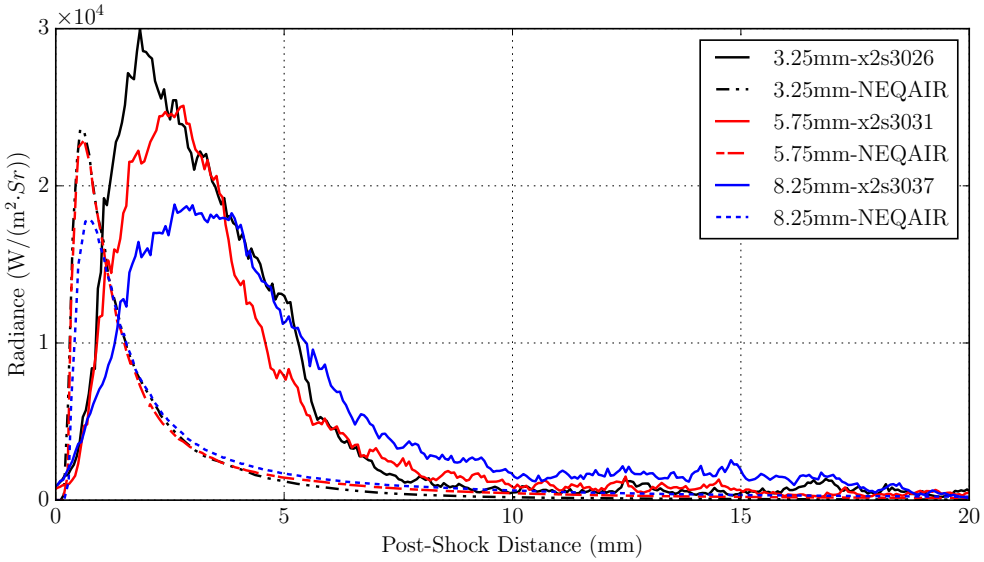

Figure 29. Radiance profiles of the 149 nm N line at 3.25, 5.75 and 8.25 mm above the top of the wedge compared between experiments and NEQAIR simulations for Condition 1

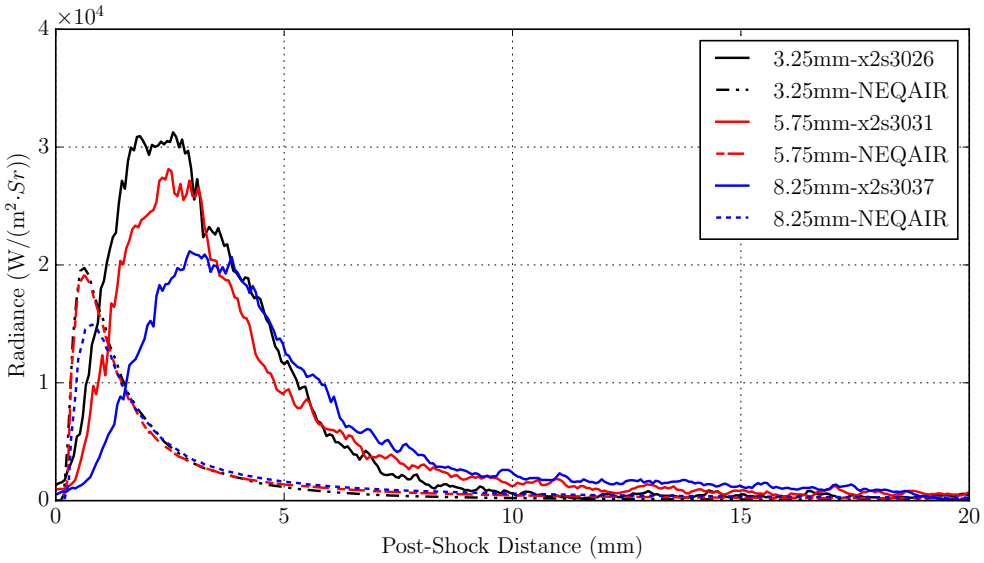

Figure 30. Radiance profiles of the 174 nm N line at 3.25, 5.75 and 8.25 mm above the top of the wedge compared between experiments and NEQAIR simulations for Condition 1

The peak radiance levels of the 149 nm line are nearly the same for the experiment and NEQAIR results at 5.75 and 8.25 mm above the wedge. The NEQAIR peak is about 20% lower than the experimental counterpart at 3.25 mm above the wedge, which can be attributed to the relatively larger departure of flow properties for shot x2s3026 from the experimentally-averaged values in Table 2. For the 174 nm N line, the peak NEQAIR results are generally about 30% lower than the experiment.

The good agreement in peak radiance levels is perhaps fortuitous, as the distance between the predicted and experiment radiance peaks increases with distance above the wedge, from 1.5 mm at 3.25 mm above

the wedge, to 2 mm and 2.5 mm further away. Note that the spans of the predicted radiance profiles are about 1.3 mm. Such a significant shift in radiance peak location suggests a serious lack of model fidelity in the excitation rate, which is not only present in the compression region right behind the shock, but also observed in the afterbody where both the 149 and 174 nm lines are heavily underpredicted.

The correlation between experiment and predicted radiance profiles and flow variables is explored along the line of sight at 8.25 mm above the wedge top where the widest VUV radiance profile and strongest afterbody radiances are observed. Such a comparison is presented for the 149 nm N line in Figure 31. Results with the 174 nm line are similar and are not shown here.

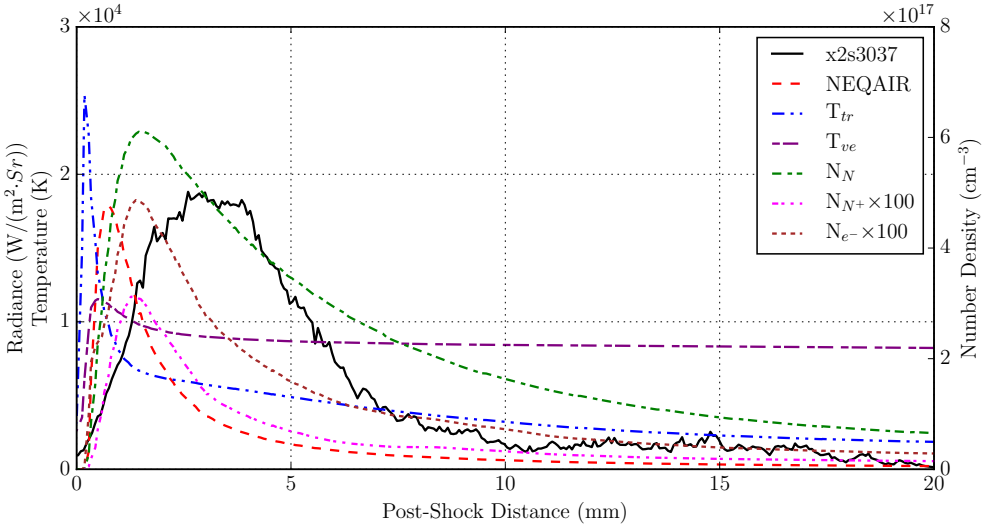

Figure 31. Experiment and NEQAIR results of the 149 nm N line, as well as selected flow variables along the line of sight at 8.25 mm above the top of the wedge for Condition 1

The NEQAIR radiance peak is less than 0.05 mm downstream from the point where T_{ve} is equal to T_{tr}. The number densities of atomic nitrogen, nitrogen ions and free electrons are still rapidly increasing past that point, and the measured 149 nm N profile continues to rise and reaches a plateau with a width of approximately 2 mm. The spans of the N, N^+ and electron number densities profile are very close to that of the 149 nm N line radiance measured, and are about three times as large as the predicted radiance profile. As the number density of a species is proportional to the product of flow density and its mass fraction in the mixture, flow density and mass fractions of relevant species are plotted along the same line of sight in Figure 32.

The spatial profiles of N, N^+ and e^- number densities shown in Figure 31 are highly synchronised with that of flow density in Figure 32. This is because the change in species mass fraction due to chemical reaction is relatively negligible compared to the change in flow density as the flow expands into the afterbody. The changes in species number density is therefore dominated by the flow expansion. For Condition 1, the ionisation level is low, and the major changes in N and N_2 mass fractions along the line of sight are due to the differences in flow properties of streamlines intersecting the line of sight at various locations. The mass fraction of atomic nitrogen is highly correlated with that of nitrogen molecule and any change in N mass fraction is reflected in the change of N_2 mass fraction in the opposite direction.

Although the mass fraction or number density of N^+ is two orders of magnitude lower than that of N, the nitrogen ions that recombine with electrons form nitrogen atoms at high-lying electronic states which emit strong VUV radiation. At the post-shock distance of about 1.4 mm where the flow starts to expand, strong recombination of N^+ proceeds and the measured 149 nm N radiance begins to approach the peak and the plateau that follows. From this point to about 6.2 mm, electronically excited nitrogen atoms are formed and radiate so strongly that the radiance levels exceed that in the shock layer. Given the serious underestimation in this region, and the fact that it is where the strongest electron-ion recombination occurs, radiation due to emission of the recombined N atom could be responsible for the mismatch between the experiments and simulations. In addition, the fact that the predicted peak is reached upstream of the experiment reflects the

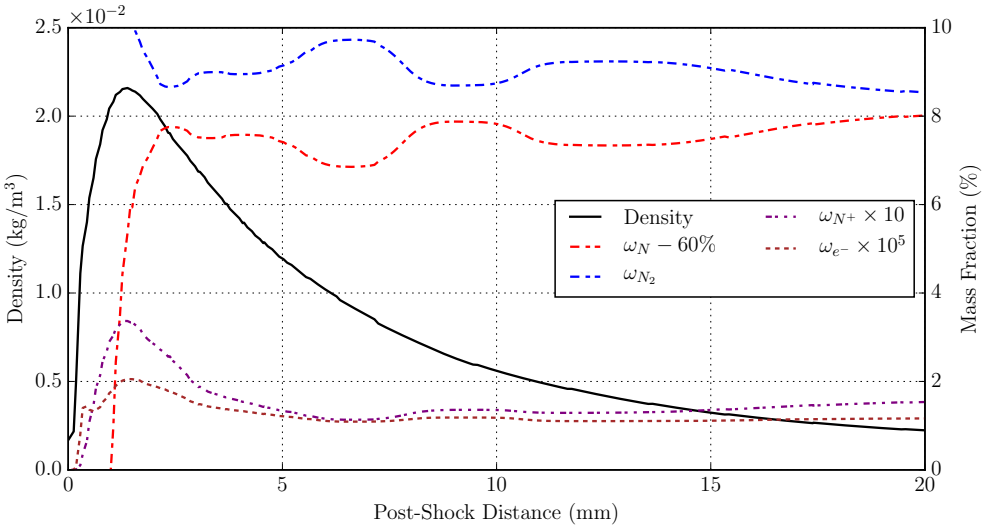

Figure 32. Density and selected species mass fraction distributions along the line of sight at 8.25 mm above the top of the wedge for Condition 1

inaccuracy in the modelling of post-shock thermal relaxation.

2. Condition 2

The 149 and 174 nm atomic nitrogen radiance profiles are compared between experiments and NEQAIR simulations and are presented in Figures 33 and 34. Similar trends observed with Condition 1 also apply to Condition 2. The measured radiances of 149 and 174 nm lines are very close to each other and so are those predicted by NEQAIR. The peak radiances predicted are lower than those measured by approximately 50% and are reached at a shorter distance behind the shock. Again, the measured radiance profiles have spans about 50% higher than those predicted by NEQAIR, and are nearly the same as those of number densities of N, N^+ and e^-, as can be observed in Figure 35.

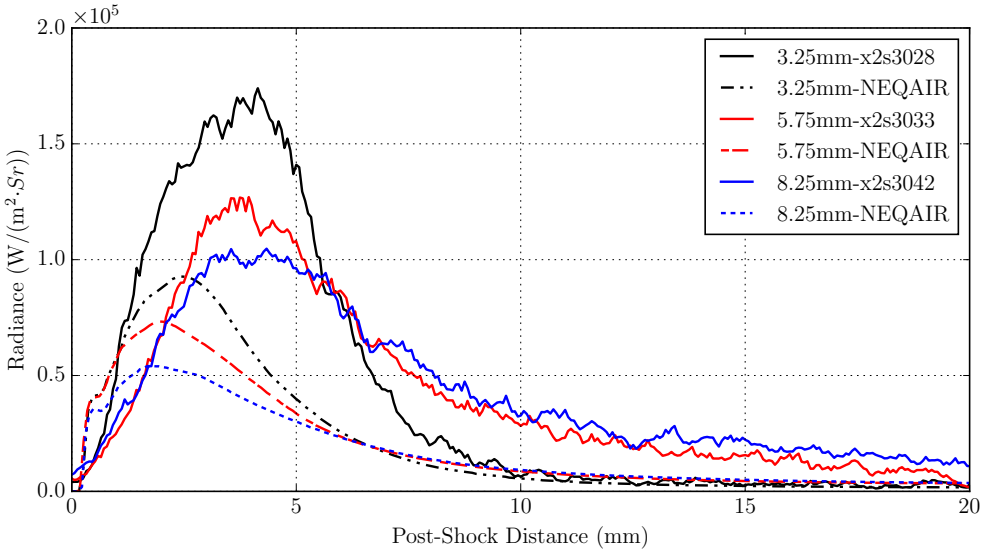

Figure 33. Radiance profiles of the 149 nm N line at 3.25, 5.75 and 8.25 mm above the top of the wedge compared between experiments and NEQAIR simulations for Condition 2

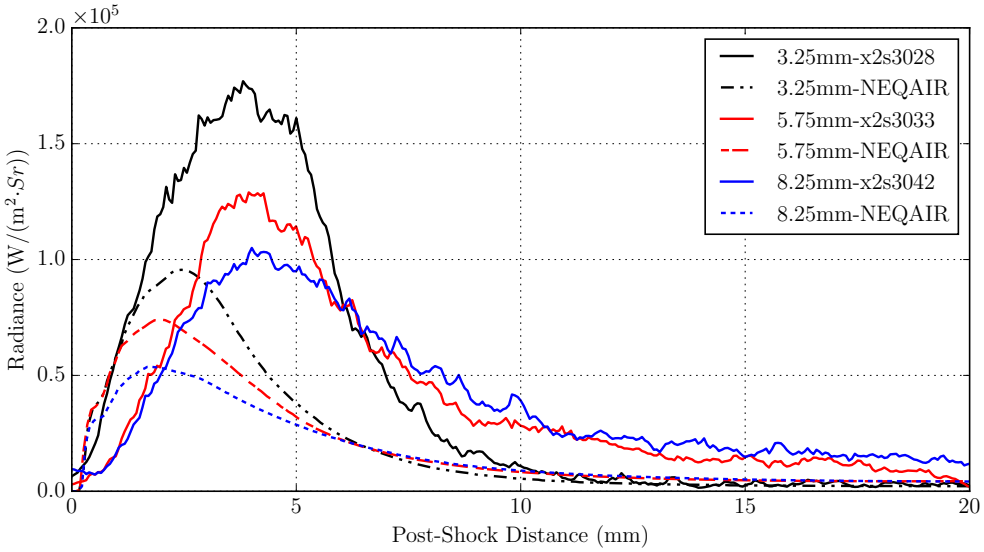

Figure 34. Radiance profiles of the 174 nm N line at 3.25, 5.75 and 8.25 mm above the top of the wedge compared between experiments and NEQAIR simulations for Condition 2

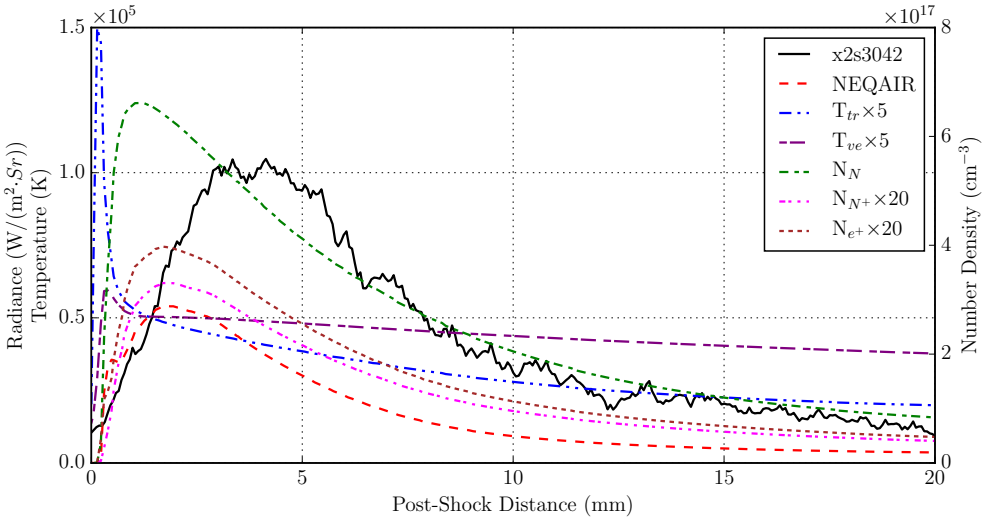

Figure 35. Experiment and NEQAIR results of the 149 nm N line, as well as selected flow variables along the line of sight at 8.25 mm above the top of the wedge for Condition 2

According to the spatial profiles of flow density and species mass fractions in Figure 36, the change in species number density for Condition 2 in the expanding flow is also dominated by the change in flow density rather than chemical reactions due to their relatively negligible contributions. The N^+ mass fraction is an order of magnitude higher than that of Condition 1. Recombination of N^+ commences at about 2.7 mm behind the shock, where the radiance of the 149 nm N lines approaches a plateau. With the depletion of N^+ comes the increase of N_2 mass fraction. With the N mass fraction found to be nearly constant downstream of its peak value, the amount of nitrogen atoms recombined into N_2 must be very close to that of those formed through the recombination of N^+ and free electrons. It is attributed to the high number density of atomic nitrogen and associated recombination rates to form nitrogen molecules.

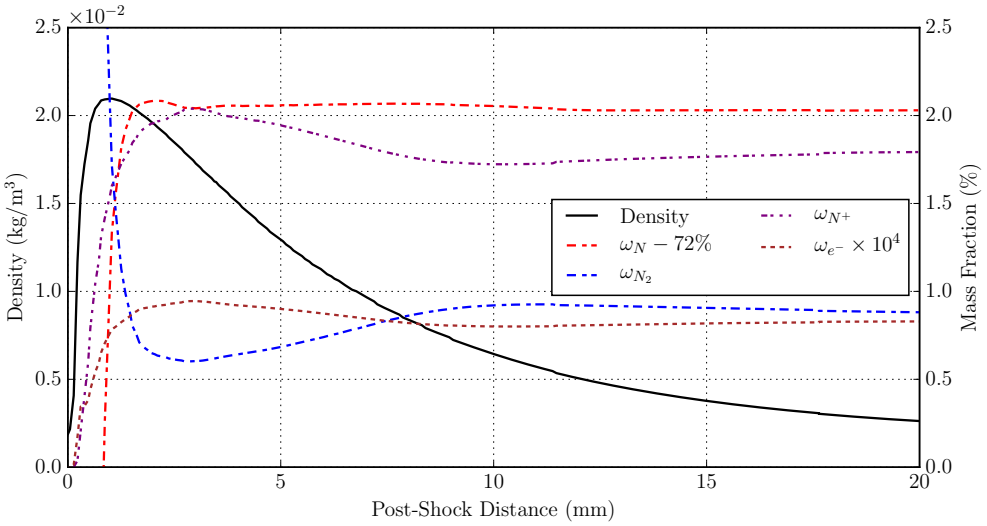

Figure 36. Density and selected species mass fraction distributions along the line of sight at 8.25 mm above the top of the wedge for Condition 2

Compared with Condition 1, the disagreement in peak radiance levels between experiment and the NEQAIR prediction is larger for Condition 2, but the relative difference in the span of the radiance profile is decreased, with that of the predicted profile only about 25% lower than the experiment value. This is attributed to the higher number densities of nitrogen ions, which are recombined to form more electronically excited nitrogen atoms that radiate in the afterbody. Similar to Condition 1, the point where N^+ starts to recombine is also where the measured radiance profile approaches a plateau. The production of nitrogen atoms at high energy states through electron-ion recombination is thought to be the reason for this plateau. Large difference still exists in the radiance values deep in the afterbody, which can be due to model deficiencies in the recombination rates and electron-impact excitation.

3. Condition 3

Figures 37 and 38 present the measured and predicted spatial profiles of 149 and 174 nm N radiances. The peak radiance is more underpredicted than Condition 2, and is lower than the experimental value by more than 60%. In the post-shock compression region, the simulated radiance profile lags behind the experimental counterpart at the same post-shock position, whereas the opposite is true for Conditions 1 and 2. This can be due to the lower density of the inflow, which leads to longer thermal relaxation distances in the simulation and consequently the predicted radiance profile that lags behind the experiment counterpart. For Conditions 1 and 2, the thermal relaxation rates could be overpredicted. The inaccuracies in electron-impact excitation rates could also be a contributing factor.

The 149 and 174 nm N profiles are also very close to each other along different lines of sight both for the experiments and the simulations. The spans of the simulation profiles underpredict the experiment values by 30%, which is quite close to the degree of underprediction for Condition 2. The measured radiance profiles for Condition 3, similar to those for the other two conditions, are of nearly the same spans with the number density profiles of N, N^+ and e^+ in Figure 39.

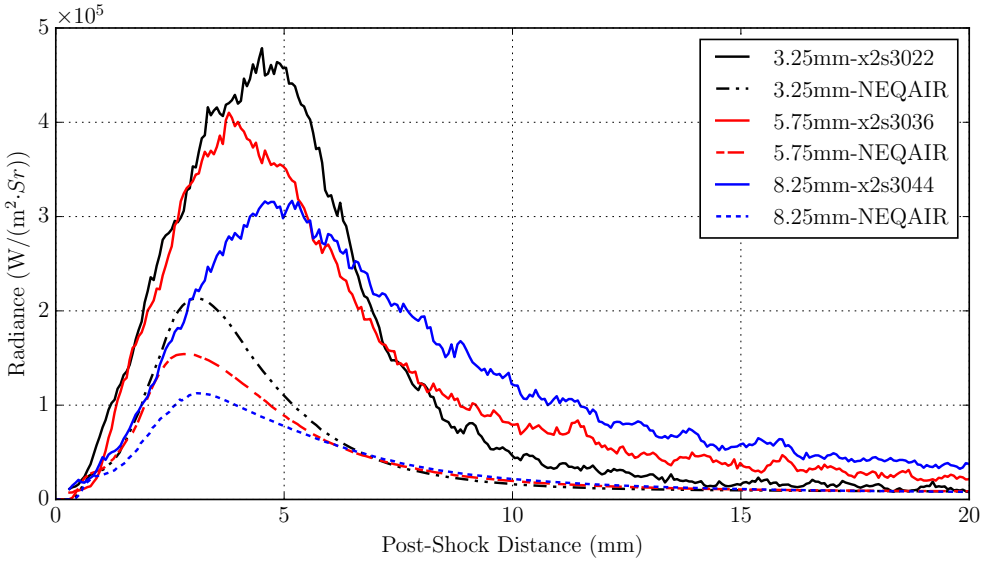

Figure 37. Radiance profiles of the 149 nm N line at 3.25, 5.75 and 8.25 mm above the top of the wedge compared between experiments and NEQAIR simulations for Condition 3

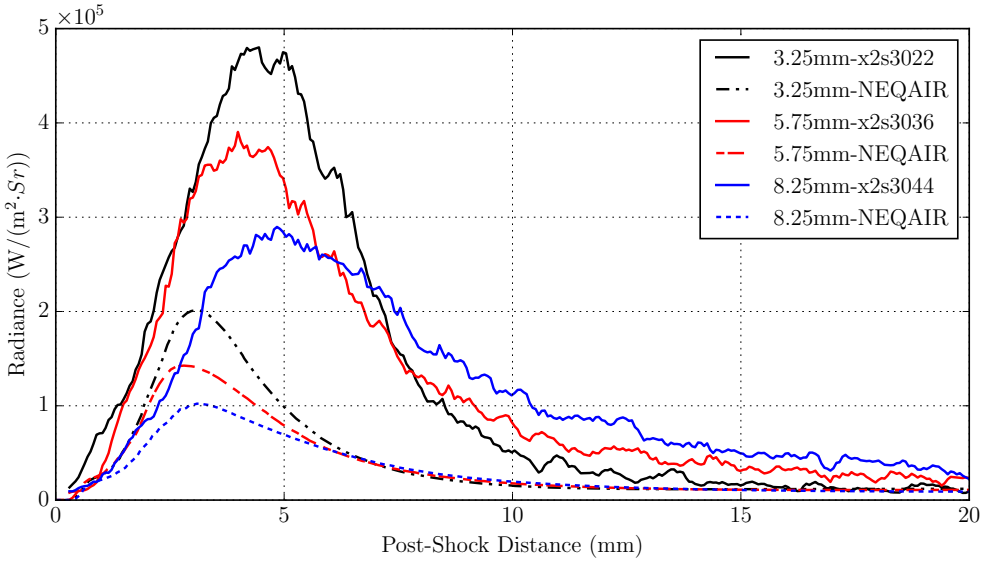

Figure 38. Radiance profiles of the 174 nm N line at 3.25, 5.75 and 8.25 mm above the top of the wedge compared between experiments and NEQAIR simulations for Condition 3

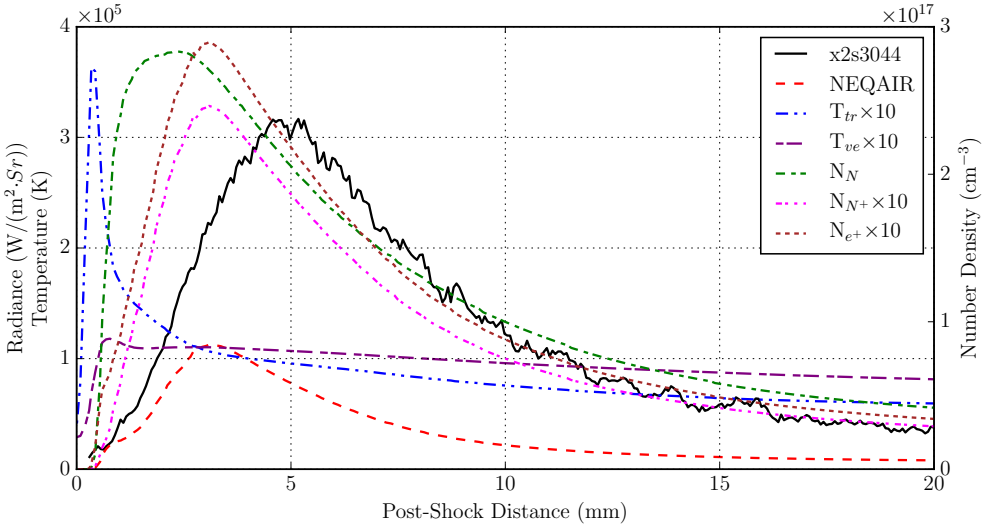

Figure 39. Experiment and NEQAIR results of the 149 nm N line, as well as selected flow variables along the line of sight at 8.25 mm above the top of the wedge for Condition 3

Similar to the other two conditions, the species spatial profiles with Condition 3 also follow that of flow density along the line of sight, as is presented in Figure 40. N_2 mass fraction is even lower than Condition 2 and stays constant until about 7 mm behind the shock as a result of higher temperatures. N_2 mass fraction reaches the minimum at about 2.4 mm away from the shock front and downstream of that point, the changes in N mass fraction are only related to that of N^+. At about 3.4 mm behind the shock, N^+ starts to recombine and the measured radiance profile is still on the rise and is 1 mm away from the peak.

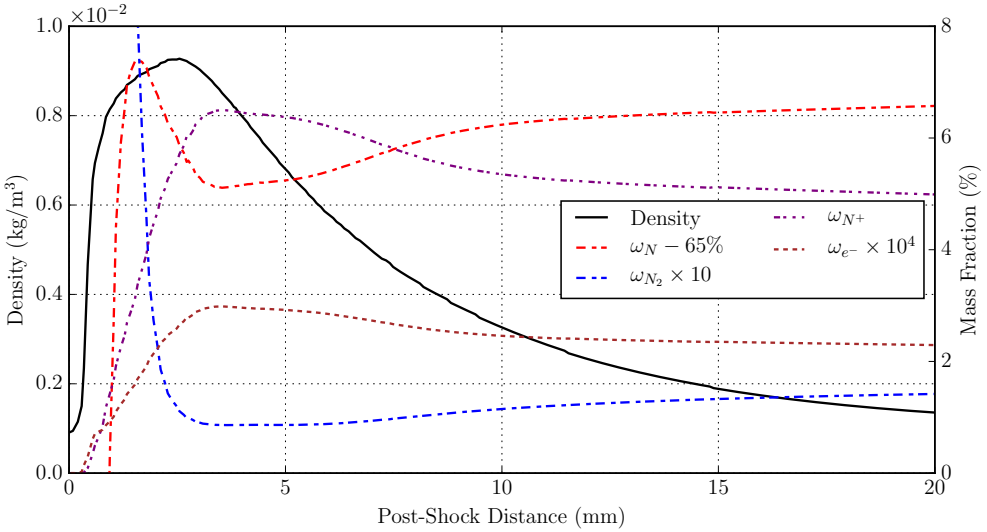

Figure 40. Density and selected species mass fraction distributions along the line of sight at 8.25 mm above the top of the wedge for Condition 3

Like Condition 2, the disagreement between experiments and simulations is relatively small between the shock front and the point where the radiance peak is predicted by NEQAIR, which could be attributed to inaccuracies in modelling post-shock relaxation and electron-impact excitation processes. Past the predicted peak radiance point, the simulation significantly departs from experiment data, and the relative differences between experiments and NEQAIR simulations are the largest downstream of the measured peak radiance

point and into the afterbody.

In summary, afterbody VUV radiation is significantly underpredicted for all three conditions. Spans of the predicted radiance profiles are smaller than the those of the measured radiance profiles. The relative width difference is the largest for Condition 1 and similar for Conditions 2 and 3. The experimental radiance profiles of N radiation in the VUV are of similar if not the same spans to those of N, N^+ and e^- number density profiles, which are found to follow the spatial profile of flow density due to limited changes in mass fractions resulting from chemical reactions in the afterbody flow.

Condition 1 has the lowest N and N^+ number densities both in the post-shock compression region and in the afterbody due to low flow temperature. The amount of N^+ recombination is of little influence on N mass fraction but is of significant impact on the afterbody radiation which is seriously underpredicted. Conditions 2 and 3 are more strongly ionised as a result of higher temperatures and share some similarities in the development of radiance profiles. For Condition 2, the recombination of N^+ and N both proceeds in the afterbody, and leads to nearly constant N mass fraction with that of N_2 increasing downstream. As the temperatures are even higher for Condition 3, N^+ mass fraction is also higher and the change in N^+ mass fraction due to recombination is directly reflected in the increase in N mass fraction in the afterbody.

The electron-ion recombination process is believed to be the main reason for significant underprediction in the afterbody radiance as the starting point of recombination coincides with the location where the differences between simulations and experiments begin to widen. The electron-impact excitation process is also considered an important factor especially deep in the afterbody, due to the resemblance of the measured radiance profile to that of the predicted electron number density.

D. Comparisons between Filtered Images with NEQAIR Simulations

Due to the weak NIR radiation with Condition 1 and insufficient sensitivity of the high speed camera, no usable filtered images have been acquired at Condition 1. Figure 41 compares the extracted 777 nm oxygen triplet radiance between experiments and NEQAIR simulations along lines of sight at varied distances above the top of the wedge for Condition 2. Good agreement within 15% is found between the shock front to 5 mm behind it for lines of sight at 3.25 and 5.75 mm away from model top. The agreement at 8.25 mm above the wedge is not as good, and the relative deviation is generally about 30% within 3.4 mm behind the shock. There is far better agreement than for the VUV lines and the spans of the predicted 777 nm triplet radiance profiles agree well with those of the measured.

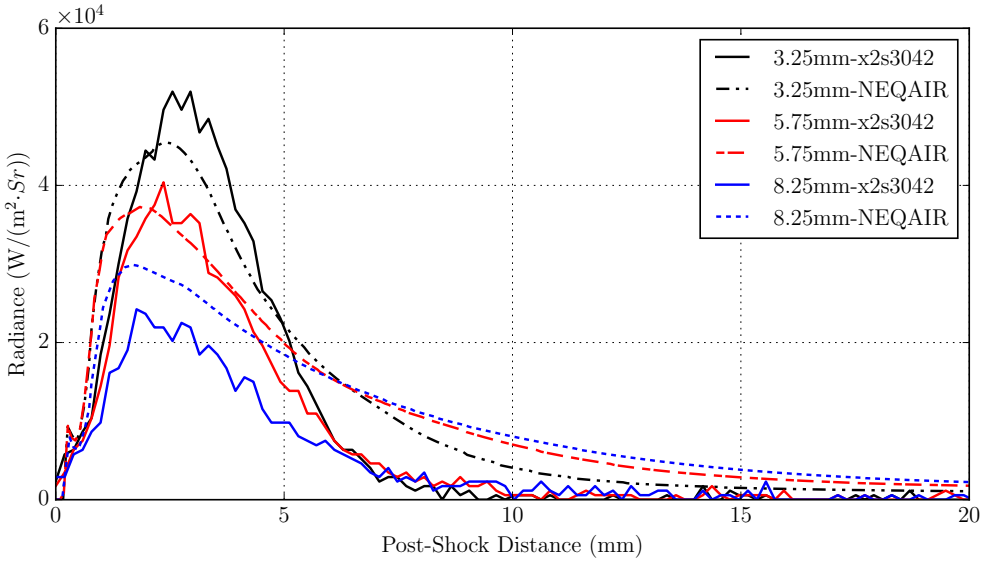

Figure 41. Radiance profiles of the 777 nm oxygen triplet at 3.25, 5.75 and 8.25 mm above the top of the wedge compared between experiments and NEQAIR simulations for Condition 2

Unlike the underpredicted VUV lines, the 777 nm oxygen triplet radiance is highly overestimated by more than a factor of two between 7.5 to 10 mm behind the shock while the measured values essentially

approach zero. Figure 42 presents the spatial profiles of flow density and associated species along the line of sight at 8.25 mm above the model. The profiles along other lines of sight exhibit similar characteristics and are not presented.

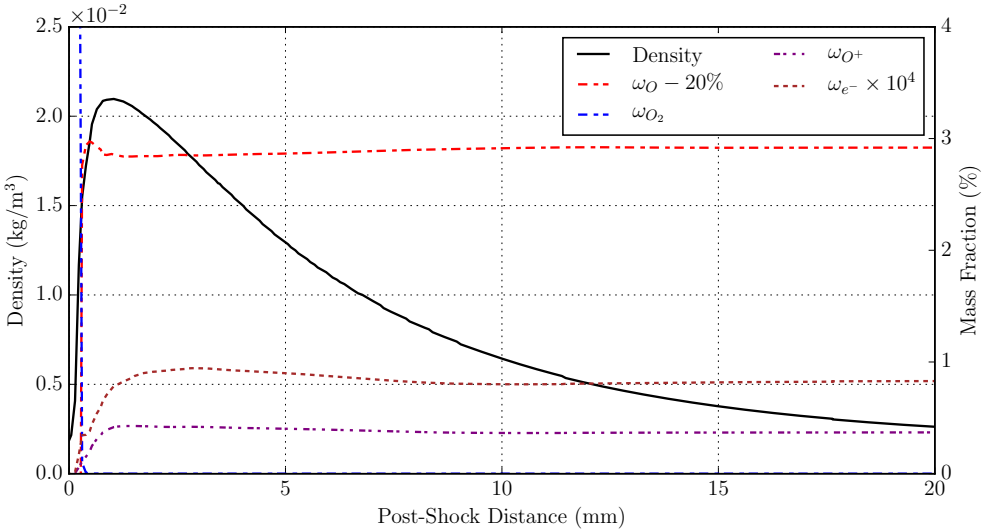

Figure 42. Density and selected species mass fraction distributions along the line of sight at 8.25 mm above the top of the wedge for Condition 2

The mass fractions of O_2, O and O^+ are frozen just prior to flow expansion, and their number density profiles will be directly determined by the flow density. The mass fraction of free electrons continues to increase by an insignificant amount at the early stage of the expansion due to the ongoing ionisation of atomic nitrogen shown in Figure 36. With little O recombined from O^+ and e^-, O at high-lying electronic states that are responsible for emission in the afterbody should originate from excitation due to collisions with other particles. Given the better agreement in the compression region and the upstream section of the expanding flow and overprediction deeper in the afterbody, and considering that the profile of predicted radiance follows that of flow density and therefore electron number density, the electron-impact excitation rates may be overestimated for O in the afterbody.

The 777 nm oxygen triplet radiance profiles are compared between NEQAIR simulations and those extracted from the filtered images in Figure 43 for Condition 3. The level of agreement between experiment and NEQAIR simulations is low for the 777 nm O line along all three lines of sight, with NEQAIR results underpredicting by as much as 40% in the peak radiance region and overpredicting by up to 100% in the afterbody. Despite the unsatisfactory levels of agreement, the spans of the predicted radiance profiles match well with those extracted from the filtered images.

In comparison with Condition 2, the level of overprediction in the afterbody is less. This is likely related to the underprediction in the compression region. Unlike the case with Condition 2 in which the mass fractions of O and O^+ become essentially frozen at a short distance behind the shock front, about 15% of the O^+ recombines between 3 and 10 mm behind the shock front, as seen in Figure 44. With the largest differences between simulations and experiments occurring from 3 to 5 mm away from the shock, and only about 3% of the O^+ recombined over the distance, the electron-ion recombination process should be of little contribution to the large disagreement.

In summary, good agreement between the NEQAIR simulations and calibrated filtered images of the 777 nm oxygen triplet has been achieved for Condition 2 in the compression region and the upstream section of the expanding flow, especially at 3.25 and 5.75 mm above the wedge top. Deeper in the afterbody, the radiance of the 777 nm O line is overpredicted by as much as a factor of two. Overestimation of electron-impact excitation is blamed for such discrepancies. For Condition 3, the agreement between experiments and simulations is worse in contrast to Condition 2 except deep in the afterbody. It's worth noting that for both conditions, the spans of the predicted radiance profiles match very well with those extracted from the filtered images. This is an important modelling improvement over results for nitrogen lines in the VUV.

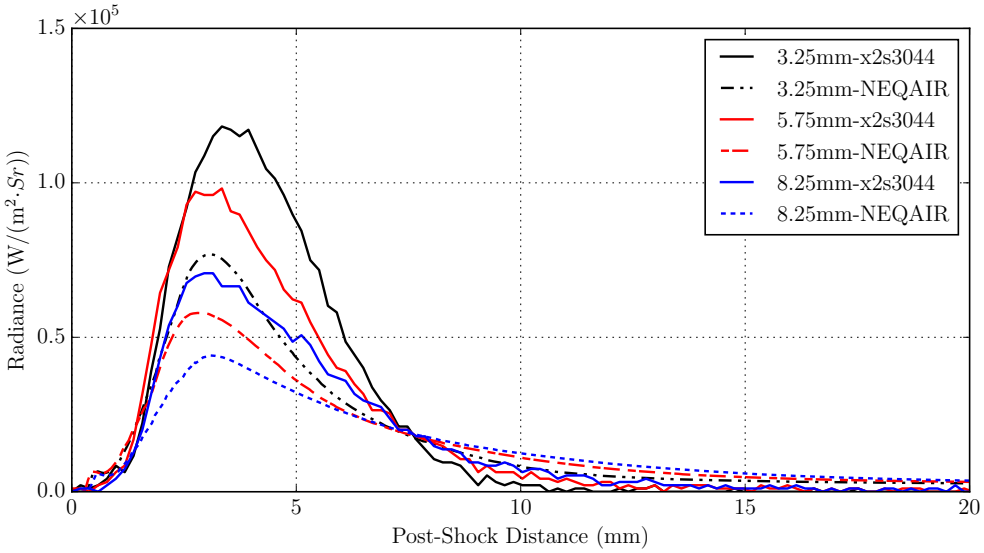

Figure 43. Radiance profiles of the 777 nm oxygen triplet at 3.25, 5.75 and 8.25 mm above the top of the wedge compared between experiments and NEQAIR simulations for Condition 3

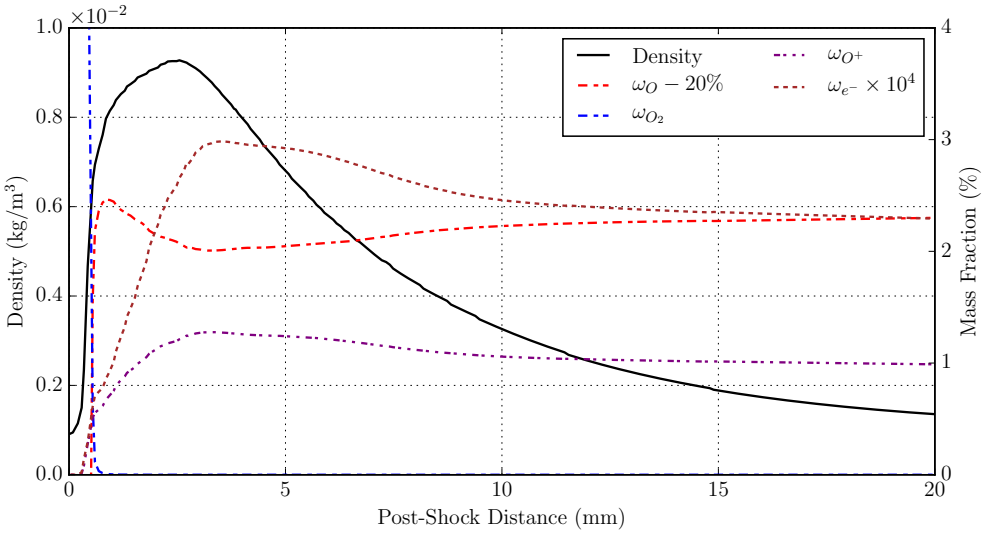

Figure 44. Density and selected species mass fraction distributions along the line of sight at 8.25 mm above the top of the wedge for Condition 3

Although slightly more recombination of O^+ occurs in the afterbody at Condition 3, the disparity could be attributed to the uncertainty or inaccuracy of inflow condition. With the highest temperature and velocity and the lowest flow density among the three flow conditions, the assumption of thermal-chemical equilibrium for the inflow may not be accurate enough due to thermochemical nonequilibrium in the nozzle. The lack of radiation coupling could also contribute to the disagreement.

V. Conclusions

A wedge model with simple geometry has proved successful in creating steady ionised expanding flow in the X2 expansion tunnel facility. Three flow conditions have been tested and the use of wall-pressure data to characterise the flow condition for individual experiments reveals the shot-to-shot variations not disclosed by measured shock speeds. VUV spectra from 118 to 180nm have been acquired both across the width and through the top surface of the wedge. The VUV spectra and calibrated images of the 777nm oxygen triplet have been analysed and compared with numerical simulations and radiation modelling with Eilmer3 and NEQAIR v14, which lead to the following conclusions:

- The spatial profiles of 149 and 174nm N radiance are in general of larger spans than those predicted by NEQAIR. For the 9.7km/s Condition 1, spans of the predicted radiance profiles are less than half of those measured. For the 10.9km/s Condition 2 and 11.8km/s Condition 3, underestimation is about 25 and 30% respectively. For all three conditions, the spans of measured 149 and 174nm N radiance profiles are nearly the same as those of the predicted number density profiles of N, N^+ and e^-. These profiles are found to follow the evolution of flow density, due to relatively negligible amount of species production and depletion as a result of chemical reactions in the afterbody.

- For Condition 1, the peak radiance levels in VUV show reasonable agreement between experiments and NEQAIR simulations. However, the predicted peak occurs at a shorter distance behind the shock, and is achieved near the point where T_{ve} is equal to T_{tr}. For Conditions 2 and 3, the peak radiance levels are significantly underestimated. Large departures of predicted radiance values from experiment appear to occur at the start of the expansion fan where the electron-ion recombination process commences, which is proposed as the main reason for the large disagreement between experiments and simulations in the afterbody.

- NEQAIR results agree well with the filtered images of 777nm oxygen triplet in the compression region and at the start of the expansion fan for Condition 2. In the afterbody, NEQAIR overpredicts by as much a factor of 3, in contrast to the strong underestimation of VUV radiation. For Condition 3, radiance in the compression region and at the start of the expansion fan are underpredicted by as much as 40%, but the afterbody radiance is overpredicted by up to 100%. With little O recombined in the afterbody, the disagreement in the afterbody is mainly attributed to inaccurate electron-impact excitation rates and that in the compression region for Condition 3 can be due to thermal non-equilibrium in the inflow and the lack of radiation coupling.

VI. Acknowledgements

The present work was funded by the Australian Research Council. Special thanks goes to Dr. Brett A. Cruden from NASA Ames Research Center who gave invaluable advice on the calibration problem. This research was undertaken with the assistance of resources from the National Computational Infrastructure (NCI), which is supported by the Australian Government. Some computations were performed on the Tinaroo computing facility, which is managed by the Research Computing Centre of the University of Queensland. The experiments wouldn't be possible without the help and input of Mechanical Engineers Frans De Beurs and Neil Duncan. The raw data file from the Shimadzu HPV-1 high speed camera could be accessed thanks to the Python library developed by Dr. Fabian Zander during his visit to the Centre for Hypersonics in December 2015. The help from Christopher James in characterising the flow conditions is highly appreciated. Tremendous thanks also goes to facility operators Christopher James, Sangdi Gu, Steven Lewis, Samuel Stennett, Timothy Cullen and Rory Kelly, who ensured the completion of the experiments.

References

[1]Olynick, D., Chen, Y.-K., and Tauber, M. E., "Aerothermodynamics of the Stardust Sample Return Capsule," *Journal of Spacecraft and Rockets*, Vol. 36, No. 3, May 1999, pp. 442–462.

[2]Yamada, T., Inatani, Y., Honda, M., and Hirai, K., "Development of thermal protection system of the MUSES-C/DASH reentry capsule," *Acta Astronautica*, Vol. 51, No. 1-9, July 2002, pp. 63–72.

[3]Johnston, C. O. and Brandis, A. M., "Features of Afterbody Radiative Heating for Earth Entry," *Journal of Spacecraft and Rockets*, Vol. 52, No. 1, 2015, pp. 105–119.

[4]Wright, M. J., Milos, F. S., and Tran, P., "Afterbody Aeroheating Flight Data for Planetary Probe Thermal Protection System Design," *Journal of Spacecraft and Rockets*, Vol. 43, No. 5, Sept. 2006, pp. 929–943.

[5]Slocumb, T. H., "Project Fire II Afterbody Temperatures and Pressures at 11.35 Kilometers Per Second," Tech. Rep. NASA TM X-1319, National Aeronautics and Space Administration, 1966.

[6]Lee, D. B. and Goodrich, W. D., "The Aerothermodynamic Environment of the Apollo Command Module during Superorbital Entry," Tech. Rep. NASA TN D-6792, National Aeronautics and Space Administration, 1972.

[7]Wright, M., Loomis, M., and Papadopoulos, P., "Aerothermal Analysis of the Project Fire II Afterbody Flow," *Journal of Thermophysics and Heat Transfer*, Vol. 17, No. 2, 2003, pp. 240–249.

[8]Johnston, C. O. and Panesi, M., "Advancements in Afterbody Radiative Heating Simulations for Earth Entry," *46th AIAA Thermophysics Conference*, AIAA Aviation, American Institute of Aeronautics and Astronautics, June 2016.

[9]Lopez, B., Johnston, C. O., and Panesi, M., "Improved Non-Boltzmann Modeling for Nitrogen Atoms," *46th AIAA Thermophysics Conference*, AIAA Aviation, American Institute of Aeronautics and Astronautics, June 2016.

[10]West, IV, T. K., Johnston, C. O., and Hosder, S., "Uncertainty and Sensitivity Analysis of Afterbody Radiative Heating Predictions for Earth Entry," *54th AIAA Aerospace Sciences Meeting*, AIAA SciTech, American Institute of Aeronautics and Astronautics, Jan. 2016.

[11]Gildfind, D. E., Morgan, R. G., and Jacobs, P. A., "Expansion Tubes in Australia," *Experimental Methods of Shock Wave Research*, edited by O. Igra and F. Seiler, Springer International Publishing, Cham, Switzerland, 2016, pp. 399–431.

[12]Gildfind, David E., *Development of High Total Pressure Scramjet Flow Conditions using the X2 Expansion Tube*, Ph.D. thesis, The University of Queensland, Brisbane, Australia, 2012.

[13]Sheikh, U. A., Morgan, R. G., and McIntyre, T. J., "Vacuum Ultraviolet Spectral Measurements for Superorbital Earth Entry in X2 Expansion Tube," *AIAA Journal*, Vol. 53, No. 12, May 2015.

[14]James, C. M., Gildfind, D., Morgan, R. G., Lewis, S. W., and Fahy, E. J., "On the Current Limits of Simulating Gas Giant Entry Flows in an Expansion Tube," *20th AIAA International Space Planes and Hypersonic Systems and Technologies Conference*, International Space Planes and Hypersonic Systems and Technologies Conferences, American Institute of Aeronautics and Astronautics, July 2015.

[15]Thornagel, R. and Kroth, S., "Deuterium Lamp with MgF2 Window Calibration Certificate," Tech. Rep. 7.2-1.21-11-03, Physikalisch-Technische Bundesanstalt, Oct. 2011.

[16]Thorne, A. P., *Spectrophysics*, Chapman and Hall, London, 2nd ed., 1988.

[17]Cruden, B. A., "Absolute Radiation Measurements in Earth and Mars Entry Conditions," *Radiation and gas-surface interaction phenomena in high-speed reentry - STO AVT-218*, University of Illinois at Urbana Champaign, IL, USA, 2014.

[18]Gollan, R. J. and Jacobs, P. A., "About the formulation, verification and validation of the hypersonic flow solver Eilmer," *International Journal for Numerical Methods in Fluids*, Vol. 73, No. 1, Sept. 2013, pp. 19–57.

[19]Program Development Corporation, "GridPro GUI Manual Version 2.1," .

[20]Park, C., "Assessment of a two-temperature kinetic model for dissociating and weakly ionizing nitrogen," *Journal of Thermophysics and Heat Transfer*, Vol. 2, No. 1, Jan. 1988, pp. 8–16.

[21]Gollan, R. J., *Computational Modelling of High-Temperature Gas Effects with Application to Hypersonic Flows*, Doctor of Philosophy, The University of Queensland, Brisbane, Australia, 2008.

[22]Potter, D. F., *Modelling of radiating shock layers for atmospheric entry at Earth and Mars*, Ph.D. thesis, The University of Queensland, Brisbane, Australia, 2011.

[23]Gupta, R. N., Yos, J. M., Thompson, R. A., and Lee, K.-P., "A review of reaction rates and thermodynamic and transport properties for an 11-species air model for chemical and thermal nonequilibrium calculations to 30000 K," Tech. Rep. NASA-RP-1232, National Aeronautics and Space Administration, 1990.

[24]Wright, M. J., Bose, D., Palmer, G. E., and Levin, E., "Recommended Collision Integrals for Transport Property Computations Part 1: Air Species," *AIAA Journal*, Vol. 43, No. 12, Dec. 2005, pp. 2558–2564.

[25]Wright, M. J., Hwang, H. H., and Schwenke, D. W., "Recommended Collision Integrals for Transport Property Computations Part 2: Mars and Venus Entries," *AIAA Journal*, Vol. 45, No. 1, Jan. 2007, pp. 281–288.

[26]Park, C., "Review of chemical-kinetic problems of future NASA missions, I - Earth entries," *Journal of Thermophysics and Heat Transfer*, Vol. 7, No. 3, Sept. 1993, pp. 385–398.

[27]Sharma, S. P., Huo, W. M., and Park, C., "Rate parameters for coupled vibration-dissociation in a generalized SSH approximation," *Journal of Thermophysics and Heat Transfer*, Vol. 6, No. 1, Jan. 1992, pp. 9–21.

[28]Gnoffo, P. A., Gupta, R. N., and Shinn, J. L., "Conservation equations and physical models for hypersonic air flows in thermal and chemical nonequilibrium," Tech. Rep. NASA TP-2867, National Aeronautics and Space Administration, 1989.

[29]Millikan, R. C. and White, D. R., "Systematics of Vibrational Relaxation," *The Journal of Chemical Physics*, Vol. 39, No. 12, Dec. 1963, pp. 3209–3213.

[30]Appleton, J. P. and Bray, K. N. C., "The conservation equations for a non-equilibrium plasma," *Journal of Fluid Mechanics*, Vol. 20, No. 04, 1964, pp. 659–672.

[31]Brandis, A. M. and Cruden, B. A., "NEQAIRv14. 0 Release Notes: Nonequilibrium and Equilibrium Radiative Transport Spectra Program," .

[32]Kramida, A., Ralchenko, Yu., Reader, J., and and NIST ASD Team, NIST Atomic Spectra Database (ver. 5.3), [Online]. Available: `http://physics.nist.gov/asd` [2016, August 21]. National Institute of Standards and Technology, Gaithersburg, MD., 2015.

[33]Cruden, B. A., Martinez, R., Grinstead, J. H., and Olejniczak, J., "Simultaneous Vacuum-Ultraviolet Through Near-IR Absolute Radiation Measurement with Spatiotemporal Resolution in An Electric Arc Shock Tube," *41st AIAA Thermophysics Conference*, Fluid Dynamics and Co-located Conferences, American Institute of Aeronautics and Astronautics, June 2009.